

NONTHERMAL SYNCHROTRON RADIATION FROM GAMMA RAY BURST EXTERNAL SHOCKS AND THE X-RAY FLARES OBSERVED WITH SWIFT

CHARLES D. DERMER

U.S. Naval Research Laboratory, Code 7653, 4555 Overlook SW, Washington, DC, 20375-5352

Draft version February 7, 2020

ABSTRACT

An analysis of the interaction between a spherical relativistic blast -wave *shell* and a stationary *cloud* with a spherical cap geometry is performed assuming that the cloud width $\Delta_{cl} \ll x$, where x is the distance of the cloud from the GRB explosion center. The interaction is divided into three phases: (1) a collision phase with both forward and reverse shocks; (2) a penetration phase when either the reverse shock has crossed the shell while the forward shock continues to cross the cloud, or vice versa; and (3) an expansion phase when, both shocks having crossed the cloud and shell, the shocked fluid expands. Temporally evolving spectral energy distributions (SEDs) are calculated for the problem of the interaction of a blast-wave shell with clouds that subtend large and small angles compared with the Doppler(-cone) angle $\theta_0 = 1/\Gamma_0$, where Γ_0 is the coasting Lorentz factor. The Lorentz factor evolution of the shell/cloud collision is treated in the adiabatic limit. Behavior of the light curves and SEDs on, e.g., Γ_0 , shell-width parameter η , and properties and locations of the cloud is examined. Short timescale variability (STV) in GRB light curves, including ~ 100 keV γ -ray pulses observed with BATSE and delayed ~ 1 keV X-ray flares found with Swift, can be explained by emissions from an external shock formed by the GRB blast wave colliding with small density inhomogeneities in the “frozen pulse” approximation ($\eta \rightarrow 0$, where $\Delta_0 + \eta x/\Gamma_0^2$ is the blast-wave shell width), and perhaps in the thin-shell approximation ($\eta \approx 1/\Gamma_0$), but not when $\eta \approx 1$. If this approximation is valid, then external shock processes could make the dominant prompt and afterglow emissions in GRB light curves, consistent with short delay two-step collapse models for GRBs.

Subject headings: gamma ray bursts — radiation processes: nonthermal — hydrodynamics — relativity

1. INTRODUCTION

Important knowledge about the nature of GRBs comes from analyses of burst light curves. BATSE, triggering on peak flux over 64, 256, and 1024 ms timescales in the 50 – 300 keV band, provides the largest database at hard X-ray/soft γ -ray energies, amounting to over 2292 GRBs reported nearly 8 years into the mission (Fishman 1999), and ~ 2700 BATSE GRBs in total. Examining BATSE GRB light curves gives the impression that the γ -ray activity, so intense during the first ~ 1 – 100 s, begins to weaken with time, all the while displaying pulses with relatively constant widths. If this evidence requires for its explanation a very powerful structured relativistic wind from an active central engine that becomes less vigorous with time, then the implied GRB explosion mechanism is very different than if this data is taken as evidence for a single explosive event where the GRB pulses are made by external shocks from a weakening blast wave that interacts with material in the circumburst medium.

The GRB afterglow revolution, initiated by Beppo-SAX and continued with HETE-2 and INTEGRAL, gave for the first time GRB source redshifts and distances and therefore apparent isotropic powers and energies. With the opening angle of the relativistic jet inferred from the achromatic beaming breaks in optical light curves, the absolute energy of a GRB is fixed to the uncertainty in the efficiency of radiation production. The tools of standard relativistic blast-wave physics for the afterglow external shock emissions allow one to test for uniform or wind-formed circumburst media, and determine the ϵ_e

and ϵ_e parameters for assumed jet structures (Panaitescu & Kumar 2002). Fitting the statistical data on the GRB redshift and opening angle distributions can determine the intrinsic jet opening angle and whether a top-hat model for GRB jet structure gives good agreement with the data (Guetta & Piran 2006; Le & Dermer 2007).

A rich new database is recently opened by Swift (Gehrels et al. 2004). After triggering with BAT in the 15 – 150 keV range, Swift autonomously slews within ≈ 100 s to a burst so that the XRT, with excellent sensitivity, can get a clear picture of the evolution of the 0.3 – 10 keV X-ray emission. In large numbers of GRBs, there are steep declines in the X-ray emission at the end of the prompt X-ray luminous phase hundreds of seconds after the start of the GRB (Tagliaferri et al. 2005), an extended plateau phase (Barthelmy et al. 2005), and X-ray flares (Burrows et al. 2005), which in some cases have durations that are a small fraction of the time since the start of the GRB. Extrapolation of the BAT into the XRT band gives an almost continuous X-ray light since the GRB trigger (O’Brien et al. 2006).

The interpretation of this data is complicated not only by the rich detail revealed by Swift but, for statistical studies, by its unusual triggering method, which makes the assignment of a threshold flux problematical (Band 2006). Because the Swift BAT uses a coded mask from which images of the GRB photons can be formed, a lower peak flux than pre-Swift telescopes can be identifiable as a GRB by using both rate and image triggers. A broader dynamic range, from 0.004 s to 26 s, is used for the rate trigger. Differences in redshift distributions of Swift GRBs compared with the GRBs detected with BATSE,

Beppo-SAX and HETE-2, which had comparable triggering criteria can, however, mainly be understood by different peak flux sensitivities of Swift and pre-Swift detectors (Le & Dermer 2007).

The X-ray flares in the late prompt and early afterglow ($t \sim 10^2$ s – 10^4 s) observed with the Swift satellite have been interpreted as evidence for internal shocks and refreshed energization of the relativistic outflow (Zhang et al. 2006). Liang et al. (2006) and Yamazaki et al. (2006) model the steeply declining phase as a superposition of background external shock emission and a curvature pulse produced by shells ejected long after the start of the GRB. This model for energy dissipation in GRBs and production of the GRB light curves is commensurate with the collapsar/failed supernova scenario for long-duration GRBs,¹ where the evolved iron core of a massive star collapses to a black hole. In the collapsar picture, energy dissipation in an accretion torus or through the Blandford-Znajek process drives a narrow collimated jet through the stellar envelope. During the early prompt phase, continued activity drives successive waves of collimated relativistic plasma through the SN shell. Collisions between the shells make GRB pulses. Later activity and peculiarities in the light curves are attributed to refreshed outflows or internal shocks from late outbursts of the engine. Interpreting rapid variations in the GRB X-ray light curve as activity of the central engine, then the engines in some GRB sources must be on for rest-frame times $\lesssim 10^4$ s after the start of the event (Burrows et al. 2005; Falcone et al. 2006; Burrows et al. 2005a).

Early calculations of the spectral and temporal behavior of the GRB pulses in an internal shock model were made by Daigne & Mochkovitch (1998), Kobayashi et al. (1997), and Granot et al. (1999). The efficiency difficulties for the internal shock model (Kumar 1999; Beloborodov 2000; Mimica et al. 2007) are reduced by large Lorentz-factor contrasts between different shells (Kobayashi & Sari 2001), which constrains the collision radius and νF_ν peak energies under the requirement of Thomson thinness (Guetta et al. 2001). For the internal shock/colliding shell model, as well as for the external shock model, efficiency concerns are ameliorated by the large hadronic energy content in the prompt phase that escapes to form the ultra-high energy cosmic rays (Dermer 2007).

A complete description of the collision between two relativistic shells that follows both the hydrodynamics and radiation physics needed to calculate emission spectra and light curves from different pulses in GRBs, necessary to test the internal shell model, seems not yet to have been accomplished (the latest internal shell models, by Mimica et al. 2005, 2007, follow hydrodynamics and internal energy dissipation in colliding shells but not particle evolution). Here we attempt a complete and systematic analysis of the collision between a cold GRB blast wave shell and a cloud with a spherical cap geometry in an external shock model, which may be used as a template for internal shell collisions. We use these results to check the widespread claims by the Swift team

¹ Long-duration GRBs are referred to henceforth as GRBs; here we do not consider the short hard GRB class or the low-luminosity GRBs, also argued to form a separate class (Liang et al. 2006a).

that central engine activity is responsible for the erratic X-ray flares from GRBs (e.g., O'Brien et al. 2006a; Falcone et al. 2006a; Romano et al. 2006; Burrows et al. 2007). We dispute these claims and argue that an external shock model can make the prompt γ -ray pulses and afterglow X-ray flares under the condition of no spreading of the cold blast-wave fluid shell. If this assumption is allowed, then interesting implications for the nature of the collapse process in GRB sources follow. A short delay two-step collapse process, in fact, provides a competing and compelling alternative to the collapsar/failed supernova model, as discussed below (Section 5).

The emissivities calculated from the interaction of a blast-wave shell and a stationary cloud are integrated over three spatial dimensions to obtain spectral fluxes as a function of observer time. Only the synchrotron component is considered here, and other assumptions are made to simplify the analysis, for example, a randomly ordered magnetic field and isotropic electron distribution in the proper frame of the shocked fluid.

The techniques of the standard blast-wave model are used (e.g. Sari et al. 1998; Piran 1999, 2005; Mészáros 2006), and the results are applied to observations of prompt ~ 100 keV emission pulses and ~ 1 keV X-ray flares in GRB light curves. The problem is analyzed and broken into three distinct interaction phases, as described in Section 2. Calculations of light curves and SEDs from the emissions of external shocks formed by the interaction of a GRB blast wave with a stationary cloud are presented in Section 3. Parameter are chosen to produce short timescale variability (STV; $\Delta t_v/\hat{t} \ll 1$, where Δt_v is the variability time scale and \hat{t} is the time since the start of the GRB) in the γ -ray lightcurve, which is only possible if the blast wave shell width can be approximated by a a thin shell ($\Delta(x) \lesssim x/\Gamma_0^3$) or frozen (unspreading) shell. This result is demonstrated analytically in Section 4, and illustrated by Monte Carlo simulations of GRB light curves. We conclude that the X-ray flares observed with Swift are compatible with an external shock model if the GRB blast wave shell interacts with a clumpy surrounding external medium and does not spread transversely. This assumption is discussed in Section 5, and is argued to be correct. Implications for the nature of the collapse mechanism and jet formation in long-duration GRBs are also discussed in Section 5. The study is summarized in Section 6.

2. ANALYSIS OF THE BLAST-WAVE/CLOUD INTERACTION

Consider a GRB that takes place at redshift z and releases energy over a characteristic timescale Δ_0/c representing the period of activity of the GRB central engine. The corresponding spatial dimension Δ_0 must, of course, be greater than the Schwarzschild radius of the several Solar mass black hole formed in the GRB event; thus $\Delta_0 \gtrsim 10^6$ cm. Depending on the nature of the central engine of GRBs, Δ_0 could range from a fraction of a second to hundreds of seconds or longer if, as in the collapsar model for the GRB prompt phase, the duration of the highly variable X-ray and γ -ray flux in a GRB is assumed to reflect the period of activity of the engine. Here we consider a GRB engine where the progenitor neutron star collapses impulsively to a black hole, so that $\Delta_0 \sim 10^7 \Delta_7$ cm, with $\Delta_7 \sim 1$.

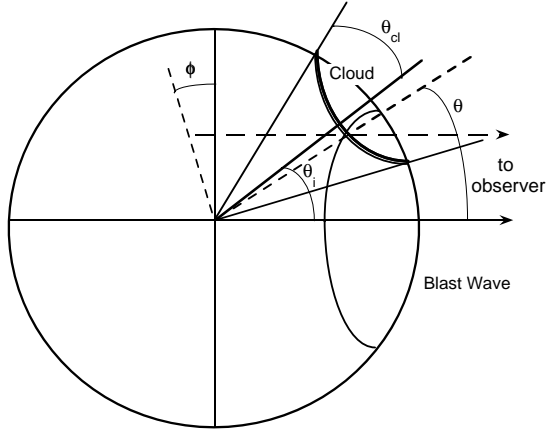


FIG. 1.— Illustration (not drawn to scale) of the geometry of a spherical, relativistic blast-wave shell interacting with a cloud having a spherical cap geometry. The axis through the center of the cloud is offset from the observer's line of sight by the angle θ_i . The cloud subtends an angle θ_{cl} as measured from the explosion center. Emission originates from radiating plasma located at a distance x from the center of the GRB explosion, and at angles θ and ϕ measured with respect to the line-of-sight direction to the observer. To approximate a quasi-spherical cloud, the transverse and lateral extents of the cloud are set equal.

The apparent isotropic equivalent γ -ray energy released by a GRB explosion is written as E_0 , in cgs units of ergs. The apparent 20 keV – 2 MeV isotropic rest-frame energy measured from GRBs typically range in values from $\approx 10^{51} - 10^{54}$ ergs, with a handful of anomalously low energy GRBs with energies as low as 10^{48} ergs (e.g., GRB 980425; Friedman & Bloom 2005; Ghirlanda et al. 2007). A significant number of GRBs have $E_0 \gtrsim 10^{54}$ ergs, so that the total GRB energy must be larger, by a factor of at least several (and possibly much larger if the radiation efficiency is low or energetic hadrons are formed and escape, e.g., as neutrons (Atoyan & Dermer 2003; Dermer 2007)). In this study, jet effects are considered as a restriction on the interaction angle, the jet structure is assumed to be ‘top-hat,’ and there is no lateral and very little transverse spreading.

The explosion is assumed to form a fireball with initial Lorentz factor (entropy per baryon) denoted by

$$\Gamma_0 = \frac{E_0}{M_0 c^2} \gg 1, \quad (1)$$

where M_0 is the amount of baryonic matter mixed into the initial explosion. In this analysis, we do not consider effects of neutron decoupling (Derishev et al. 1999; Bahcall & Mészáros 2000; Beloborodov 2003), and furthermore assume that the blast-wave energy in the coasting stage is carried primarily by particle rather than field energy (see, e.g., Lyutikov & Blackman 2001, for the latter case).

The blast-wave plasma shell reaches its coasting Lorentz factor Γ_0 at distance $x \gtrsim \Gamma_0 \Delta_0$ from the explosion. At $x \gtrsim x_{spr} \equiv \Gamma_0^2 \Delta_0$, where x_{spr} is the spreading radius, internal motions within the blast-wave shell² are thought to cause it to spread so that $\Delta(x) \approx \eta x / \Gamma_0^2$

² The relativistic blast-wave shell from the GRB will always be referred to as the *shell*, and the stationary material that is swept up by the shell will be referred to as a *cloud*, even when the cloud represents supernova remnant (shell) material.

(Mészáros et al. 1993; Piran 1999), where $\eta \lesssim 1$. We consider the case that the shell experiences little spreading, so that $\eta \ll 1$, which has as its asymptotic limit the frozen-pulse approximation ($\eta \rightarrow 0$). More discussion about η and shell spreading is given in Section 4.4.

In the stationary frame of the explosion, the shell width $\Delta(x)$ is therefore given by

$$\Delta(x) \cong \Delta_0 + \eta \frac{x}{\Gamma_0^2}, \quad (2)$$

and the proper number density of the relativistic shell is given by

$$n(x) = \frac{E_0}{4\pi x^2 \Gamma_0^2 m_p c^2 \Delta(x)}. \quad (3)$$

2.1. Geometry of the Blast Wave/Cloud Interaction

The interaction event is sketched in Fig. 1. The blast-wave shell of width $\Delta = \Delta(x_0)$ collides with a uniform cloud with density n_{cl} . The cloud is assumed to have a spherical cap geometry and to subtend a solid angle $\Delta\Omega_{cl} = \pi\theta_{cl}^2$ as measured from the explosion center, and therefore presents a projected area $A_{cl} = \pi\theta_{cl}^2 x_0^2$ to the GRB blast wave, where x_0 is the distance from the origin to the inner edge of the cloud. The angle between the axis through the cloud center and the line-of-sight to the observer is denoted θ_i . The coordinates $\vec{x} = (x, \theta, \phi)$ defining the location of the radiating material in the stationary (explosion) frame are measured with respect to the line-of-sight to the observer, with the angle ϕ representing the projection of the azimuth on the plane normal to the direction to the observer; thus $\phi = 0$ is defined with respect to the projection of the axis through the cloud center on this plane (see Fig. 1a). For simplicity, both the shell and cloud are assumed to be composed of electron-proton plasma.

The νF_ν flux, denoted by $f_\epsilon(t)$, measured at observer time t and at dimensionless photon energy $\epsilon = h\nu/m_e c^2$, is given by

$$f_\epsilon(t) = d_L^{-2} \int_0^{2\pi} d\phi \int_{-1}^1 d\mu \int_0^\infty dx x^2 \epsilon' j'(\epsilon', \vec{\Omega}'; \vec{x}, t') \delta_D^3, \quad (4)$$

where primes refer to comoving quantities, $\epsilon' = \epsilon_z / \delta_D \equiv (1+z)\epsilon / \delta_D$, and the integration is over volume in the stationary (explosion) frame (Granot et al. 1999; Kumar & Panaiteescu 2000; Dermer 2004). The Doppler factor of the radiating fluid is defined by the expression

$$\delta_D = \frac{1}{\Gamma(1 - \beta\mu)}, \quad (5)$$

where $\mu = \cos\theta$, $\Gamma = \Gamma(\vec{x}, t_*)$ is the emitting fluid's Lorentz factor, and $\beta c = c\sqrt{1 - \Gamma^{-2}}$ is its speed. The differential emissivity

$$j'(\epsilon', \vec{\Omega}'; \vec{x}, t') = \frac{d\mathcal{E}'(\vec{\Omega}')}{dV' dt' d\Omega' d\epsilon'}$$

is defined such that $j'(\epsilon', \vec{\Omega}'; \vec{x}, t') dV' dt' d\Omega' d\epsilon'$ is the differential comoving energy $d\mathcal{E}'$ of photons with dimensionless energies between ϵ' and $\epsilon' + d\epsilon'$ that are radiated during time dt' from comoving volume dV' within the solid angle element $d\Omega'$ in the direction $\vec{\Omega}'$ defined in the comoving fluid frame. Although the directional properties of the radiation must be considered in the general

case of nonthermal synchrotron emission from relativistic electrons in an ordered magnetic field, or for external Compton processes, here we assume that the radiation is emitted isotropically in the comoving frame, and assume a nonthermal synchrotron origin for the keV – MeV emission from GRBs. Implicit in this approximation is that the magnetic field is randomly ordered and that the electrons have an isotropic pitch angle distribution in the fluid frame.

Thus $j'(\epsilon', \vec{\Omega}'; \vec{x}, t') = j'(\epsilon'; \vec{x}, t')/4\pi$. Because the azimuthal dependence no longer appears in either $j'(\epsilon'; \vec{x}, t')$ or δ_D , it is trivial to integrate eq. (4) over ϕ under the assumption that the emissivity $j'(\epsilon'; \vec{x}, t') = j'(\epsilon'; x, t')$, that is, the emissivity depends only on x and t but not on angle (except as determined by the physical extent of cloud). This assumption allows us to treat the hydrodynamics of the blast-wave/cloud interaction in a planar geometry (Section 2.2). We obtain

$$f_\epsilon(t) = (2\pi d_L^2)^{-1} \int_{\theta_i - \theta_{cl}}^{\theta_i + \theta_{cl}} d\theta |\sin \theta| \phi_+ \times \int_0^\infty dx x^2 \epsilon' j'(\epsilon'; x, t') \delta_D^3, \quad (6)$$

noting that the Doppler factor is, in general, dependent on location. The term $\phi_+ = \phi_+(\theta, \theta_{cl}, \theta_i)$ represents the maximal azimuthal angle subtended by the cloud for received emission from radiating plasma located at an angle θ with respect to the observer's line of sight; see Fig. 1. From the addition formula for angles in spherical geometry, we have that $\cos \theta_{cl} = \cos \theta \cos \theta_i + \sin \theta \sin \theta_i \cos \phi_+$. Inspection of Fig. 1 reveals that when $\theta_i < \theta_{cl}$, that is, when the line of sight to the observer intersects the cloud volume, then $\phi_+ = \pi$ when $\theta \leq \theta_{cl} - \theta_i$. Thus we have two cases, as follows:

1. $\theta_i < \theta_{cl}$

$$\phi_+ = \begin{cases} \pi, & \text{when } \theta_i - \theta_{cl} \leq \theta \leq \theta_{cl} - \theta_i, \\ \arccos \Theta, & \text{when } \theta_{cl} - \theta_i \leq \theta \leq \theta_i + \theta_{cl} \\ 0, & \text{otherwise; and} \end{cases} \quad (7)$$

2. $\theta_i > \theta_{cl}$

$$\phi_+ = \begin{cases} \arccos \Theta, & \text{when } \theta_i - \theta_{cl} \leq \theta \leq \theta_{cl} + \theta_i, \\ 0, & \text{otherwise,} \end{cases} \quad (8)$$

where

$$\Theta \equiv \frac{\cos \theta_{cl} - \cos \theta \cos \theta_i}{\sin \theta \sin \theta_i}.$$

The stationary frame time t_* is related to the observer time t through

$$t_z \equiv \frac{t}{(1+z)} = t_* - \frac{x \cos \theta}{c}, \quad (9)$$

where the zero of time in the two frames is defined by the start of the GRB explosion. The differential distance dx traveled by a relativistic blast wave during the differential time elements dt_* , dt' and dt_x in the stationary, comoving, and observer frames, respectively, is given by

$$dx = \beta c dt_* = \beta \Gamma c dt' = \beta \Gamma \delta_D c dt_z. \quad (10)$$

Eqs. (9) and (10) are needed to determine the emissivity at assigned values of x and t_z .

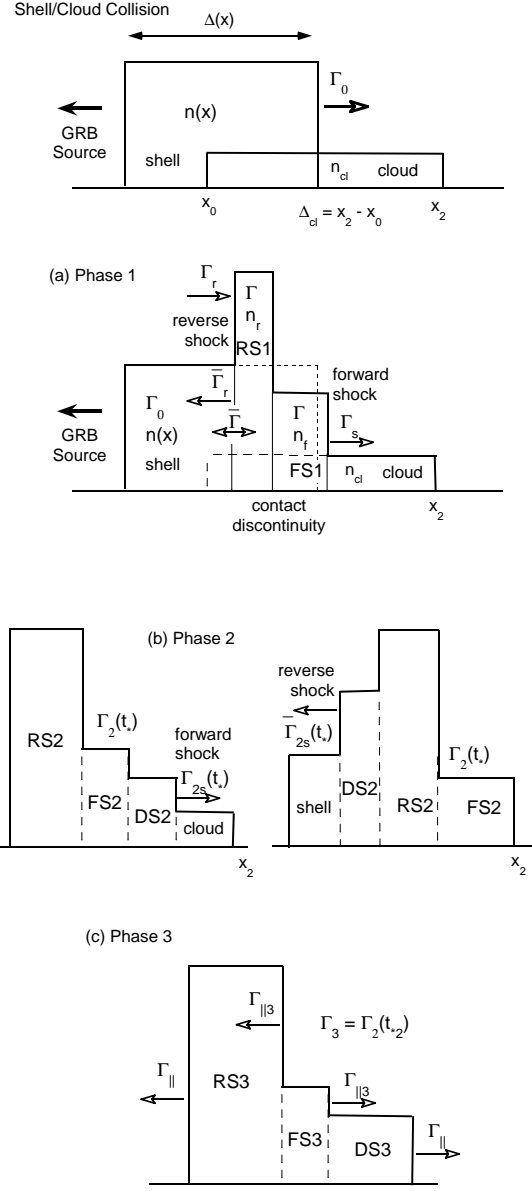


FIG. 2.— Phases of the Interaction Event. Top figure illustrates the planar geometry and widths, in the stationary frame, of the shell and cloud. Panel (a) illustrates the Collision Phase, Phase 1, with both forward shock (FS) and reverse shock (RS). Panel (b) illustrates the Penetration Phase, Phase 2, when either the RS has traversed the shell and the FS continues to pass through the cloud (left), or when the FS has traversed the cloud and the RS continues to pass through the shell (right). Panel (c) illustrates the Expansion Phase, Phase 3, where the shock fluid expands and the nonthermal particles cool, for the former (left) case of Phase 2.

2.2. Phases of the Interaction Event

The complete interaction is treated in a planar geometry, as illustrated in Figs. 1 and 2. The cloud is assumed to have uniform density between radii x_0 and x_2 , so that the cloud width $\Delta_{cl} = x_2 - x_0$. A major simplifying assumption of the analysis is that $\Delta_{cl} \ll x_0$, so that $n(x) \approx n(x_0)$ throughout the duration of the interaction.

Three phases of the interaction event are identified and illustrated in Fig. 2.

1. Collision Phase (Fig. 2a). Both a forward shock (FS) and reverse shock (RS) are found in this phase; the forward shock accelerates the cloud material, and the reverse shock decelerates the shell material.
2. Penetration Phase (Fig. 2b). This phase bifurcates into two cases, depending on whether the RS crosses the shell before the FS crosses the cloud, or whether the FS crosses the cloud before the RS crosses the shell. In the former case, the shocked fluid produced during the collision phase decelerates as more cloud material is swept up at the FS, during which time a new accelerated particle population is introduced at the decelerating forward shock, so we denote this process the deceleration shock (DS). In the latter case, the shocked fluid produced during the collision phase is accelerated by the remaining shell material at the RS, and a new particle population is accelerated at the RS. We only treat the first case of this phase (which is the most important case for GRB studies) in this paper.
3. Expansion Phase (Fig. 2c). After the FS crosses the remaining cloud material in the first case of Phase 2, or the RS crosses the remaining shell material in the second case of Phase 2, the shocked fluid, being composed of highly relativistic particles and magnetic fields, expands and adiabatically cools.

2.2.1. Collision Phase

We follow the approach of Sari & Piran (1995) and Kobayashi et al. (1999) to analyze this phase. Let $\bar{\Gamma} = 1/\sqrt{1 - \bar{\beta}^2}$ represent the relative Lorentz factor of unshocked shell material in the rest frame of the shocked fluid. From Fig. 2b,

$$\bar{\Gamma} = \Gamma\Gamma_0(1 - \beta\beta_0) \cong \frac{1}{2} \left(\frac{\Gamma}{\Gamma_0} + \frac{\Gamma_0}{\Gamma} \right), \quad (11)$$

where the last relation applies in the regime $\Gamma_0, \Gamma \gg 1$ considered here. Note that Γ and $\bar{\Gamma}$ remain constant during the duration of Phase 1, as a consequence of the assumption that $\Delta_{cl} \ll x$.

The shocked fluid travels with Lorentz factor Γ , and the shock itself moves with Lorentz factor Γ_s . When $\Gamma \gg 1$, then $\Gamma_s \cong \sqrt{2}\Gamma$, implying a compression ratio of 4Γ (particle densities will always be referred to the proper frame). Likewise, when $\bar{\Gamma} \gg 1$, the Lorentz factor of the RS in the comoving fluid frame is $\bar{\Gamma}_r \cong \sqrt{2}\bar{\Gamma}$. When $\bar{\Gamma} - 1 \ll 1$, then $\bar{\beta}_r = \sqrt{1 - \bar{\Gamma}_r^{-2}} \cong 4\bar{\beta}/3$, implying a compression ratio $\cong 4$. Thus $\bar{\Gamma}_r \cong \sqrt{2}\bar{\Gamma}$ when $\bar{\Gamma} > \sqrt{2}$, and $\bar{\beta}_r \cong 4\bar{\beta}/3$ when $\bar{\Gamma} \leq \sqrt{2}$. The Lorentz factor of the reverse shock in the stationary frame is $\Gamma_r = \Gamma\bar{\Gamma}_r(1 - \beta\bar{\beta}_r)$, and $\beta_r = \sqrt{1 - \Gamma_r^{-2}}$.

When $\Gamma \gg 1$, the fluid density of the FS material is $n_f \cong 4\Gamma n_{cl}$. The density of the reverse-shocked fluid is $n_r \cong (4\Gamma + 3)n(x)$ for a relativistic reverse shock, and $n_r \cong (4 + 5\bar{\beta}^2/4)n(x)$ for a nonrelativistic reverse shock composed of cold shell material; an expression that joins

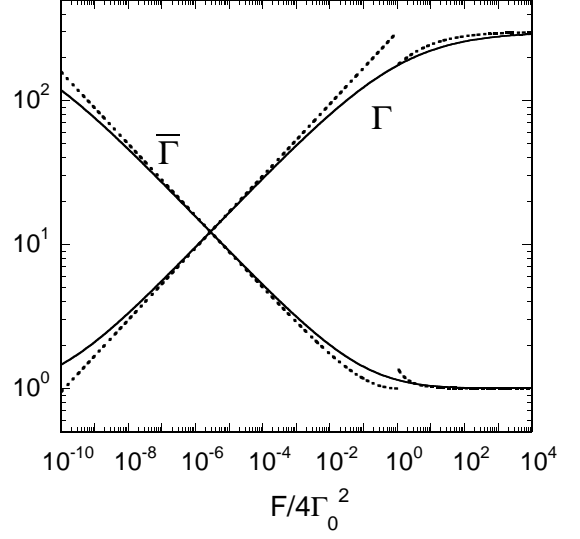


FIG. 3.— Lorentz factor Γ of the shocked fluid in the explosion frame, and Lorentz factor $\bar{\Gamma}$ of the unshocked shell material in the rest frame of the shocked fluid, as a function of $F/4\Gamma_0^2$ when $\Gamma_0 = 300$. Solid curves give numerical results, and dotted curves show approximations given in eqs. (14) and (15).

the two regimes is $n_r \approx 4\bar{\Gamma}n(x)$. The equality of kinetic-energy densities at the contact discontinuity implies that

$$n_f(\Gamma - 1) = n_r(\bar{\Gamma} - 1) \cong 4n_{cl}\Gamma^2 \cong 4n(x)(\bar{\Gamma}^2 - \bar{\Gamma}). \quad (12)$$

The relativistic shock jump conditions for an isotropic explosion in a uniform CBM therefore give (Sari & Piran 1995; Panaiteescu & Mészáros 1999)

$$\frac{n(x_0)}{n_{cl}} \equiv F = \frac{E_0}{4\pi x_0^2 \Gamma_0^2 n_{cl} m_p c^2 \Delta(x_0)} \cong \frac{\Gamma^2}{\bar{\Gamma}^2 - \bar{\Gamma}} \rightarrow \begin{cases} 2\Gamma^2/\bar{\beta}^2, & \text{Nonrelativistic RS (NRS)} \\ \Gamma^2/\bar{\Gamma}^2, & \text{Relativistic RS (RRS)} \end{cases} \quad (13)$$

Hence

$$\bar{\beta} \cong \Gamma_0 \sqrt{\frac{2}{F}}, \quad \bar{\Gamma} = \frac{1}{\sqrt{1 - \bar{\beta}^2}}, \quad \Gamma \cong \frac{\Gamma_0}{(1 + \bar{\beta})}, \quad (14)$$

when $F \gg 4\Gamma_0^2$ (NRS),

and

$$\bar{\beta} \cong 1, \quad \bar{\Gamma} = \frac{\Gamma}{\sqrt{F}}, \quad \Gamma = \frac{\Gamma_0 F^{1/4}}{\sqrt{2\Gamma_0 - F^{1/2}}} \cong \sqrt{\frac{\Gamma_0}{2}} F^{1/4}, \quad (15)$$

when $F \ll 4\Gamma_0^2$ (RRS).

Fig. 3 shows the shocked fluid Lorentz factor Γ and the relative Lorentz factor $\bar{\Gamma}$ as a function of $F/4\Gamma_0^2$ for $\Gamma_0 = 300$. The accurate numerical results are shown by the solid curves, obtained by solving $F = \beta(\Gamma^2 - \Gamma)/\bar{\beta}(\bar{\Gamma}^2 - \bar{\Gamma})$. The dotted curves show the approximate analytic expressions, eqs. (14) and (15), using the expression $\Gamma \cong \sqrt{\Gamma_0/2}F^{1/4}$ in the latter case. The numerical solutions for Γ and $\bar{\Gamma}$ are used in subsequent calculations.

The FS power is $dE'/dt'|_{FS} = A_{cl} n_{cl} m_p c^3 \beta(\Gamma^2 - \Gamma) \cong A_{cl} n_{cl} m_p c^3 \Gamma^2$. The reverse shock power is $dE'/dt'|_{RS} = A_{cl} n(x_0) m_p c^3 \bar{\beta}(\bar{\Gamma}^2 - \bar{\Gamma})$. Thus $(dE'/dt'|_{RS})/(dE'/dt'|_{FS}) = 1$, so that equal power is

dissipated as internal energy in the FS and the RS. The comoving duration of the FS before penetrating the cloud is $\Delta t'_{FS} \cong \Delta_{cl}/\Gamma c$. The comoving duration of the RS before penetrating the shell is $\Delta t'_{RS} \approx \Gamma_0 \Delta / \bar{\beta} \bar{\Gamma} c$. Thus case (1), where the RS crosses the shell before the FS crosses the cloud, applies when $\Delta t'_{RS}/\Delta t'_{FS} < 1$, that is, when $\Delta/\Delta_{cl} < \bar{\beta} \bar{\Gamma}/\Gamma_0 \Gamma \lesssim 1/\Gamma_0$. Case (1) generally applies when $\Delta \ll x/\Gamma_0^2$ (eq. [2]) and $\Delta_{cl} \lesssim x/\Gamma_0$, which is the condition for STV.

The range of x occupied by the FS fluid during phase 1 (designated as FS1) at time $t_* = t_z + x \cos \theta/c$ is

$$x_0 + \beta c(t_* - t_{*0}) \leq x \leq x_0 + \beta_s c(t_* - t_{*0}), \quad (16)$$

while the range occupied by the RS fluid during phase 1, or RS1, is

$$x_0 + \beta_r c(t_* - t_{*0}) \leq x \leq x_0 + \beta c(t_* - t_{*0}), \quad (17)$$

where $t_{*0} \equiv x_0/\beta_0 c$ and $\beta_s = \sqrt{1 - \Gamma_s^{-2}}$. The comoving time $t' = (t_{*0}/\Gamma_0) + (t_* - t_{*0})/\Gamma$, so that the elapsed comoving time since the start of the interaction is $\Delta t' = (t_* - t_{*0})/\Gamma$. In the absence of an interaction, the shell occupies the range $\beta_0 c t_* - \Delta \leq x \leq \beta_0 c t_*$. Thus the RS leaves the shell when $\beta_0 c t_* - \Delta = x_0 + \beta_r c(t_* - t_{*0})$, that is, when

$$t_* = t_{*0} + \frac{\Delta}{(\beta_0 - \beta_r)c}. \quad (18)$$

This represents the end of Stage 1 for the case where the RS crosses the shell before the FS crosses the cloud. Therefore Stage 1 lasts for comoving time

$$\Delta t'_{RS} = \frac{\Delta}{\Gamma(\beta_0 - \beta_r)c}, \quad (19)$$

which may be compared with the approximation previously derived. The time measured between the start of the GRB explosion and when the blast wave first encounters the cloud is

$$t_0 = (1+z) \frac{x_0}{\beta_0 c} \times \begin{cases} 1 - \beta_0 & \text{for } \theta_i \leq \theta_{cl}, \\ 1 - \beta_0 \cos(\theta_i - \theta_{cl}) & \text{for } \theta_i > \theta_{cl}. \end{cases} \quad (20)$$

Following the treatment of Sari et al. (1998) (for the accuracy of this approach, see Dermer et al. 2000), we let $n'(\gamma; x, t') d\gamma$ represent the differential number density of electrons with Lorentz factors between γ and $\gamma + d\gamma$ in the shocked fluid. Assuming that all swept-up electrons are accelerated by the FS with spectral index p_f , joint normalization of number and power gives a minimum electron Lorentz factor

$$\gamma_{min,f} \cong \epsilon_{e,f} \frac{m_p}{m_e} f(p_f) (\Gamma - 1), \quad \text{where } f(p) \equiv \left(\frac{p-2}{p-1} \right) \quad (21)$$

and $\epsilon_{e,f}$ represents the fraction of swept-up FS power carried by the injected nonthermal electrons (subscript “*f*” refers to the FS, and subscript “*r*” to the RS). For electrons accelerated by the RS with spectral index p_r , similar considerations give a minimum Lorentz factor

$$\gamma_{min,r} \cong \epsilon_{e,r} \frac{m_p}{m_e} f(p_r) (\bar{\Gamma} - 1). \quad (22)$$

Electrons cool through synchrotron losses during comoving time $\Delta t'$ since the start of the collision to cooling Lorentz factor

$$\gamma_{c,f} = \frac{6\pi m_e c}{\sigma_T B_f^2 \Delta t'} \quad \text{and} \quad \gamma_{c,r} = \frac{6\pi m_e c}{\sigma_T B_r^2 \Delta t'} \quad (23)$$

for the FS and RS fluids, respectively, assuming dominant synchrotron losses. The magnetic field strength B in the FS and RS fluids is assigned according to the usual prescription, namely that the magnetic-field energy density is proportional to the downstream energy density of the shocked fluid with proportionality constant $\epsilon_B \lesssim 1$. Thus

$$\begin{aligned} B_f^2 &= 32\pi n_{cl} m_p c^2 \epsilon_{B,f} \beta(\Gamma^2 - \Gamma), \quad \text{and} \\ B_r^2 &= 32\pi n(x) m_p c^2 \epsilon_{B,r} \bar{\beta}(\bar{\Gamma}^2 - \bar{\Gamma}). \end{aligned} \quad (24)$$

The maximum electron Lorentz factor γ_{max} is determined by equating the most rapid acceleration rate expected in Fermi processes, $\dot{\gamma}_{acc} = \epsilon_2 e B / m_e c$, where the rate factor $\epsilon_2 \lesssim 1$, with the synchrotron loss rate $|\dot{\gamma}_{syn}|$, giving

$$\gamma_{max,f} \cong \left(\frac{6\pi e \epsilon_{2,f}}{\sigma_T B_f} \right)^{1/2} \cong \frac{1.2 \times 10^8 \epsilon_{2,f}}{\sqrt{B_f(\text{G})}}, \quad (25)$$

and similarly for $\gamma_{max,r}$ at the RS.

We calculate the nonthermal synchrotron radiation in the collision phase spectrum by noting that the emissivity in eq. (4) can be expressed through the relation

$$\epsilon' j'(\epsilon', \vec{\Omega}'; x, t') \cong \frac{4}{3} c \sigma_T U_B \gamma_s^3 n'(\gamma_s; x, t'), \quad (26)$$

where $U_B = B^2/8\pi$ is the magnetic-field energy density,

$$\gamma_s \cong \sqrt{\frac{\epsilon_z}{\delta_D(B/B_{cr})}}, \quad (27)$$

and the critical magnetic field $B_{cr} = m_e^2 c^3 / e \hbar = 4.414 \times 10^{13}$ G. This follows from the formula for the electron energy-loss rate through synchrotron emission, and from the expression for the mean energy of synchrotron photons radiated by an electron with Lorentz factor γ_s . Eq. (26) applies to the FS and RS fluids by using values of B and γ_s appropriate to each component.

Assuming that the electrons are accelerated by the first-order Fermi shock process and injected into the shocked fluid in the form of a power law with index p , then the density distribution $n'(\gamma; x, t')$ of energized electrons can be approximated by the expression

$$\begin{aligned} \gamma n'(\gamma; x, t') &\cong \\ \frac{n(x, t')}{s-1} &\begin{cases} (\gamma/\gamma_0)^{s-1} & \text{for } \gamma_0 \leq \gamma \leq \gamma_1, \\ (\gamma_1/\gamma_0)^{1-s} (\gamma/\gamma_1)^{-p} & \text{for } \gamma_1 \leq \gamma \leq \gamma_{max}. \end{cases} \end{aligned} \quad (28)$$

In the slow-cooling regime, $\gamma_{min} < \gamma_c$, $\gamma_0 = \gamma_{min}$, $\gamma_1 = \gamma_c$, and $s = p$. In the fast-cooling regime, $\gamma_c < \gamma_{min}$, $\gamma_0 = \gamma_c$, $\gamma_1 = \gamma_{min}$, and $s = 2$ (Sari et al. 1998). At energies $\epsilon \leq \epsilon_0 = (B/B_{cr}) \gamma_0^2 \delta_D / (1+z)$, corresponding to $\gamma \leq \gamma_0$, the synchrotron spectrum is approximated by the elementary synchrotron emissivity spectrum ($\propto \epsilon^{1/3}$ in a νF_ν representation). Thus we can include this branch of the synchrotron spectrum by writing

$$\gamma n'(\gamma; x, t') \cong \frac{n(x, t')}{s-1} \left(\frac{\epsilon}{\epsilon_0} \right)^{1/3} \quad \text{for } \gamma \leq \gamma_0.$$

Synchrotron self-absorption is neglected here, which is valid for radiations detected at infrared frequencies and higher considered in this paper.

The proper densities of electrons swept up by the FS and RS are

$$n_f(x, t') = \frac{n_{cl}}{(\beta_s - \beta)} \cong 4\Gamma n_{cl} \quad \text{and} \quad n_r(x, t') = \frac{\bar{\beta} \bar{\Gamma} n(x)}{(\beta - \beta_r) \Gamma^2}, \quad (29)$$

respectively. In the treatment used here, the total electron density is independent of location within the volume of the FS and RS fluids during Phase 1. The collision phase spectrum is calculated by substituting eq. (26) into eq. (6), making use of eq. (27) to relate γ to the received photon energy.

2.2.2. Penetration Phase

Only the case where the RS passes through the shell before the FS passes through the cloud is analyzed here. During this phase, the shell is assumed to be hydrodynamically connected so that the entire shocked fluid decelerates with the same Lorentz factor Γ_2 . As the FS passes through the remaining cloud material, it sweeps up and injects a new nonthermal particle population in addition to the nonthermal electrons left over from Phase 1. We denote $\Gamma = \Gamma_1$, the Lorentz factor of the shocked fluid during Phase 1. The equation for blast-wave deceleration of a relativistic blast wave when it sweeps up material from the cloud is given by

$$\Gamma_2(x) = \frac{\Gamma_1}{[1 + (2 - \varphi)\Gamma_1^2 c^2 m(x)/E_0]^{1/(2-\varphi)}} \quad (30)$$

(Böttcher & Dermer 2000; Dermer & Humi 2001), where φ is the fraction of swept-up energy that is radiated, and $m(x) = 4\pi m_p \int_{x_\Delta}^x dx' x'^2 n_{cl}(x') \cong 4\pi m_p n_{cl} x_\Delta^2 (x - x_\Delta)$ is the swept-up mass. Here

$$x_\Delta = x_0 + \frac{\beta_s \Delta}{\beta_0 - \beta_r} \quad (31)$$

is the distance of the FS from the explosion center at the end of Phase 1 (see eqs. [16] and [18]). Defining the deceleration radius x_d through the expression $\Gamma_1 m(x_d) = E_0/\Gamma_1 c^2$ gives the following expression for the deceleration radius for a blast-wave/cloud interaction:

$$x_d = x_\Delta + \frac{E_0}{4\pi m_p c^2 \Gamma_1^2 n_{cl} x_\Delta^2}. \quad (32)$$

Assuming adiabatic evolution ($\varphi \ll 1$), eq. (30) becomes

$$\Gamma_2 = \frac{\Gamma_1}{\sqrt{1 + 2(\frac{x-x_\Delta}{x_d-x_\Delta})}} = \frac{\Gamma_1}{\sqrt{1 + 2\beta_{1s}u - u^2/2\Gamma_1^2}}, \quad (33)$$

where $u \equiv c(t_* - t_{*0})/(x_d - x_\Delta)$, and $\beta_{1s} = \sqrt{1 - 1/2\Gamma_1^2}$. The expression on the right-hand-side of eq. (33) is obtained by integrating $dx = \beta_{2s}(x)dt_*$, where $\Gamma_{2s}(x) = \sqrt{2}\Gamma_2(x)$.

During Phase 2, the particles injected at the RS and FS during Phase 1 are no longer subject to further acceleration. We assume that these fluid volumes, denoted RS2 and FS2, respectively, neither expand nor contract during Phase 2, and decelerate with Lorentz factor $\Gamma_2(t_*)$. The range occupied by RS2 is therefore

$$x_0 + \frac{\beta_r \Delta}{\beta_0 - \beta_r} + x_2(t_* - t_{*0}) \leq x \leq x_0 + \frac{\beta_1 \Delta}{\beta_0 - \beta_r} + x_2(t_* - t_{*0}). \quad (34)$$

For FS2, the range is

$$x_0 + \frac{\beta_1 \Delta}{\beta_0 - \beta_r} + x_2(t_* - t_{*0}) \leq x \leq x_\Delta + x_2(t_* - t_{*0}). \quad (35)$$

Here

$$x_2(t_* - t_{*0}) = c \int_{t_{*0}}^{t_*} dt'_* \beta_2(t'_*) = \frac{(x_d - x_\Delta)}{\Gamma_1} \left[\left(\frac{u'}{2} - \beta_{1s} \Gamma_1^2 \right) \sqrt{\frac{u'^2}{2\Gamma_1^2} - 2\beta_{1s}u' + \Gamma_1^2 - 1} \right. \\ \left. - \frac{\Gamma_1^3}{\sqrt{2}} \ln \left| \frac{\sqrt{2}}{\Gamma_1} \sqrt{\frac{u'^2}{2\Gamma_1^2} - 2\beta_{1s}u' + \Gamma_1^2 - 1} + \frac{u'}{\Gamma_1^2} - 2\beta_{1s} \right| \right]_0^u. \quad (36)$$

The elapsed comoving time since the start of Phase 2, obtained by integrating $dt' = dt_*/\Gamma_2(t_*)$, is given by

$$t' - t'_\Delta = \frac{x_d - x_\Delta}{c\Gamma_1} \left\{ \left(\frac{u}{2} - \beta_{1s} \Gamma_1^2 \right) \sqrt{1 + \beta_{1s}u - \frac{u^2}{2\Gamma_1^2}} + \beta_{1s} \Gamma_1^2 - \sqrt{2}\Gamma_1^3 [\arcsin(\beta_{1s} - \frac{u}{2\Gamma_1^2}) - \arcsin \beta_{1s}] \right\}. \quad (37)$$

The RS2 and FS2 emissivities are the same as the RS1 and FS1 emissivities, except now $\Delta t' = t' - t'_\Delta + (t_{*0} - t_0)/\Gamma_1$ is used to evaluate the cooling Lorentz factor, eq. (23). Moreover, because injection and subsequent particle acceleration has ceased in these two phases, the maximum electron Lorentz factor decays by synchrotron losses to a value of

$$\gamma_{2,f}(t') = [\gamma_{max,f}^{-1} + \frac{\sigma_T B_f^2}{6\pi m_e c} (t' - t'_\Delta)]^{-1}, \quad (38)$$

where $\gamma_{max,f}$ is given by eq. (25) for FS2, with a related equation for RS2. Because the FS and RS fluid shells are assumed not to expand during Phase 2, the magnetic field remains the same as in Phase 1.

The fluid containing the nonthermal electrons and protons injected by the decelerating shock as it sweeps up cloud material in Phase 2, denoted DS2, occupies the range

$$x_\Delta + x_2(t_* - t_{*0}) \leq x \leq x_\Delta + x_{2s}(t_* - t_{*0}), \quad (39)$$

where

$$x_{2s}(t_* - t_{*0}) = c \int_{t_{*0}}^{t_*} dt'_* \beta_{2s}(t'_*) = \frac{(x_d - x_\Delta)}{\sqrt{2}\Gamma_1} \left[\left(\frac{u}{2} - \beta_{1s} \Gamma_1^2 \right) \sqrt{\frac{u^2}{2\Gamma_1^2} - 2\beta_{1s}u + 2\Gamma_1^2 - 1} + \beta_{1s} \Gamma_1^2 \sqrt{2\Gamma_1^2 - 1} \right]. \quad (40)$$

The DS2 emissivity at time t_* , determined by the values of θ , x , and observer time t_z in the evaluation of eq. (6), is produced by nonthermal electrons injected at location x_i and time t_{*i} . The values of x_i and t_{*i} are determined by the intersection of $x_{2s} = x_\Delta + x_{2s}(t_{*i} - t_{*0})$, representing the leading edge of the deceleration shock (DS) that injects particles into the fluid, and $x_i = x - x_2(t_* - t_{*i})$, representing the worldline connecting the injection coordinates to the received values. The injection coordinates x_i and $u_i = c(t_{*i} - t_{*0})/(x_d - x_\Delta)$ are therefore obtained by numerically solving $x - x_\Delta - x_2(t_* - t_{*0}) =$

$x_{2s}(t_{*i} - t_{*\Delta}) - x_2(t_{*i} - t_{*\Delta})$ using a staggered leapfrog routine.

The received spectrum during Phase 2 is given by eq. (6), with the x -integral limited to the ranges defined above. The emissivity for DS2 is given by eq. (26), with values of γ_{min} , γ_c and γ_{max} appropriate to the injection value of $\Gamma(t_{*i})$. The elapsed comoving time since injection used to calculate γ_c is obtained from eq. (37). The Doppler factor at time t_* uses eq. (33) for Γ . Phase 2 ends when $x = x_2$, that is, at stationary time

$$t_{*2} = t_{*\Delta} + \frac{\sqrt{2}\Gamma_1(x_d - x_\Delta)}{c} \left[\sqrt{2\Gamma_1^2 - 1} - \sqrt{2\Gamma_1^2 - 1 - 2\left(\frac{x_2 - x_\Delta}{x_s - x_\Delta}\right)} \right]. \quad (41)$$

2.2.3. Expansion Phase

After the FS passes through the cloud, the shocked fluid has Lorentz factor

$$\Gamma_3 = \Gamma_2(t_{*2}) = \frac{\Gamma_1}{\sqrt{1 + 2\left(\frac{x_2 - x_\Delta}{x_d - x_\Delta}\right)}}. \quad (42)$$

Because there is no further pressure on the fluid, the shocked fluid is assumed to expand outward along the parallel direction with speed $\beta_{\parallel}c$ and Lorentz factor

$$\Gamma_{\parallel} = 1/\sqrt{1 - \beta_{\parallel}^2}.$$

(Because the shocked fluid has a much smaller parallel than transverse extent, due to the compression of the quasi-spherical cloud material by a factor $\gtrsim 4\Gamma_3$ in the parallel direction, effects of transverse expansion can be neglected.) No further injection or acceleration takes place in Phase 3, and the relativistic electrons cool by synchrotron and expansion losses. The shocked fluid in Phase 3, denoted by RS3, FS3, and DS3, consists of fluid from the prior RS, FS, and DS phases. In order that each fluid phase is to have the same fractional volume expansion, the FS fluid is assumed to expand in both transverse directions in the comoving frame with speed $\beta_{\parallel}c/3$, where $\Gamma_{\parallel 3} = 1/\sqrt{1 - (\beta_{\parallel}/3)^2}$.

From these assumptions, we define the four stationary frame Lorentz factors $\Gamma_{RS3} = \Gamma_3\Gamma_{\parallel}(1 - \beta_3\beta_{\parallel})$, $\Gamma_{FS3-} = \Gamma_3\Gamma_{\parallel 3}(1 - \beta_3\beta_{\parallel 3})$, $\Gamma_{FS3+} = \Gamma_3\Gamma_{\parallel 3}(1 + \beta_3\beta_{\parallel 3})$ and $\Gamma_{DS3} = \Gamma_3\Gamma_{\parallel}(1 + \beta_3\beta_{\parallel})$, along with their associated β factors β_{RS3} , β_{FS3-} , β_{FS3+} and β_{DS3} , respectively, that characterize the motions of the radial boundaries of the different fluid layers. The range of RS3 at time t_* is

$$\begin{aligned} x_0 + \frac{\beta_r\Delta}{\beta_0 - \beta_r} + x_2(t_{*2} - t_{*\Delta}) + c\beta_{RS3}(t_* - t_{*2}) &\leq x \\ \leq x_0 + \frac{\beta_1\Delta}{\beta_0 - \beta_r} + x_2(t_{*2} - t_{*\Delta}) + c\beta_{FS3-}(t_* - t_{*2}). \end{aligned} \quad (43)$$

For FS3, the range is

$$\begin{aligned} x_0 + \frac{\beta_1\Delta}{\beta_0 - \beta_r} + x_2(t_{*2} - t_{*\Delta}) + c\beta_{FS3-}(t_* - t_{*2}) &\leq x \\ \leq x_\Delta + x_2(t_{*2} - t_{*\Delta}) + c\beta_{FS3+}(t_* - t_{*2}). \end{aligned} \quad (44)$$

The range of DS3 is

$$x_\Delta + x_2(t_{*2} - t_{*\Delta}) + c\beta_{FS3+}(t_* - t_{*2}) \leq x$$

$$\leq x_\Delta + x_{2s}(t_{*2} - t_{*\Delta}) + c\beta_{DS3}(t_* - t_{*2}). \quad (45)$$

Let $R'_{\parallel}(t') = R'_{\parallel}^0 + 2\beta_{\parallel}ct'$ denote the comoving parallel width of the entire shocked fluid, with additional subscripts $i = \text{``RS,''} \text{``FS,''} \text{ and ``DS''}$ to refer to the widths $R'_{\parallel i}(t') = R'_{\parallel i}^0 + \frac{2}{3}\beta_{\parallel}c(t' - t'_2)$ of the forward, reverse, and deceleration shocked fluid layers, respectively. The superscript “0” refers to the radial width of the fluid layer at the end of Phase 2, and t'_2 is the comoving time at the end of Phase 2. From eqs. (43) – (45), $R'_{\parallel RS}^0 = \Gamma_3(\beta_1 - \beta_r)\Delta/(\beta_0 - \beta_r)$, $R'_{\parallel FS}^0 = \Gamma_3(\beta_s - \beta_r)\Delta/(\beta_0 - \beta_r)$, and $R'_{\parallel DS}^0 = \Gamma_3[x_{2s}(t_{*2} - t_{*\Delta}) - x_2(t_{*2} - t_{*\Delta})]$, with R'_{\parallel}^0 equal to the sum of these three widths.

Conservation of magnetic flux for the transverse magnetic-field component B_{\perp}^0 implies $B_{\perp}R_{\parallel}^2 = \text{const} = B_{\perp}^0R_{\parallel}^0$, so that $B_{\perp}(t') = B_{\perp}^0R_{\parallel}^0/[(R_{\parallel}^0 + \frac{2}{3}\beta_{\parallel}c(t' - t'_2))^2]$. If the electrons are isotropized on time scales short compared to the cooling timescale, then the electron energy loss-rate due to adiabatic and synchrotron losses is given by

$$-\frac{d\gamma}{dt'} = \frac{1}{R'_{\parallel}} \frac{dR'_{\parallel}}{dt'} \gamma + \frac{\sigma_T[B_{\perp}^2(t') + B_{\parallel}^2(t')]}{6\pi m_e c} \gamma^2, \quad (46)$$

where B_{\parallel} is the parallel magnetic-field component. Assuming that $B_{\perp}(t') \gg B_{\parallel}(t')$, which would occur if the magnetic field is formed by sweeping up and compressing an external field, then eq. (46) can be written in the form

$$-\frac{d\gamma}{d\tau} = \frac{\gamma}{\tau} + b\frac{\gamma^2}{\tau^4}, \quad (47)$$

where $\tau \equiv 1 + \frac{2}{3}\beta_{\parallel}c(t' - t'_2)/R_{\parallel}^0$ and $b \equiv R_{\parallel}^0\sigma_T B_{\perp}^0/[(4\pi\beta_{\parallel}m_e c^2)]$. This can be solved (Gupta et al. 2006) using the substitution $y = \gamma\tau^{-n}$, with $n = 3$, giving the result

$$\gamma(\tau) = \frac{4\tau^3}{b(\tau^4 - 1) + 4\tau^4/\gamma_i}, \quad (48)$$

where γ_i is the initial electron Lorentz factor at $t' = t'_2$ or $\tau = 1$.

The emissivity for RS3 and FS3 is given by eq. (26) with

$$n'(\gamma; t') = n'(\gamma; \tau) = \left[\frac{R_{\parallel}(t')}{R_{\parallel}^0} \right]^{-1} \frac{n'(\gamma_i; 1)\gamma_i^2}{\tau\gamma^2} = \frac{n'(\gamma_i; 1)\gamma_i^2}{\tau^2\gamma^2}, \quad (49)$$

$B \rightarrow B_{\perp}(t') = B_{\perp}^0/\tau^2$, and $n'(\gamma_i; 1)$ is the electron γ distribution at the end of Phase 2. This expression also applies to the DS3 emissivity, with the emission coordinates x, t_* mapped back to the injection coordinates x_i, t_{*i} as was done for DS2. Note the minor inconsistency for Phase 3 between the original assumption that the magnetic field is randomly ordered, compared to the dominant perpendicular magnetic field component implied by field compression in this phase. This inconsistency should be relaxed with the use of directional synchrotron emissivity spectra in more detailed treatments but, in either case, the contribution from the expansion phase is usually much smaller than that from the penetration phase. The Doppler factor during Phase 3 is $\delta_D = [\Gamma_3(1 - \beta_3\mu)]^{-1}$.

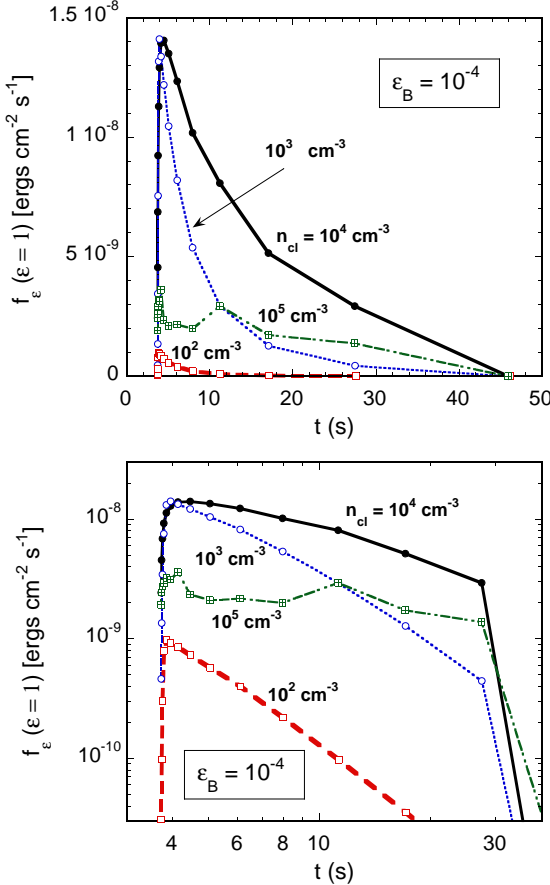


FIG. 4.— Lightcurves calculated at 511 keV for a standard model GRB pulse with $\epsilon_B = 10^{-4}$ and $\eta = 1/\Gamma_0$. The cloud geometry is fixed with $\theta_{cl} = 3/\Gamma_0$, but its density is varied as labeled by the curves. Top panel: linear scale. Bottom panel: logarithmic scale.

3. RESULTS

Nonthermal synchrotron emission spectra from blast-wave/cloud interactions were computed using the formulae given in the previous section. Standard parameters are given in Table 1. For the model GRB pulse, we consider a source at $z = 1$, corresponding to the mean redshift of the pre-Swift BATSE/Beppo-SAX/HETE-2/INTEGRAL sample. The coasting Lorentz factor and apparent isotropic energy release of the blast wave are chosen to be $\Gamma_0 = 300$ and $E_0 = 10^{53}$ ergs, respectively. The initial width of the shell is $\Delta_0 = 10^7$ cm. The blast wave is assumed to encounter a small cloud with nominal density $n_{cl} = 10^3$ cm $^{-3}$ located at a distance $x_0 = 10^{16}$ cm from the explosion center³ centered along the line-of-sight to the observer. To simulate a quasi-spherical cloud, the cloud width $\Delta_{cl} = 2 \times 10^{14}$ cm and $\theta_{cl} = 0.01$. Other standard parameters are injection electron index $p = 2.5$, $\epsilon_e = 0.1$, and $\epsilon_2 = 0.1$. The parameters $\epsilon_e, \epsilon_B, \epsilon_2$, and p of the FS and RS are assumed to be the same throughout all phases of the interaction in the calculations presented here.

Fig. 4 shows lightcurves computed at 511 keV for the standard model GRB pulse with $\epsilon_B = 10^{-4}$. We prove in Section 4.2 that a rapidly variable bright pulse cannot be made when $\eta = 1$, and numerical simulations with

³ The total mass of such clouds distributed in all directions around the GRB source is $\lesssim 10^{-5} M_\odot$.

$\eta = 1$ confirm this result. Thus we adopt the thin-shell assumption ($\eta = 1/\Gamma_0$) in Fig. 4, and assume that the cloud is on the axis to the line-of-sight to the observer. This calculation shows the dependence of the behavior of the light curve on cloud density n_{cl} .

The kinematic minimum and maximum times are implied by the idealized cloud location and geometry. From eq. (20) for on-axis clouds,

$$t_{min} = t_{z0} \equiv \frac{(1+z)x_0}{2\Gamma_0^2 c} \cong 3.70 \left(\frac{1+z}{2} \right) \frac{x_{16}}{\Gamma_{300}^2} \text{ s}$$

and $t_{max} \approx t_{min}(1 + \Gamma_0^2 \theta_{cl}^2)$; (50)

depending on observing energy, the maximum emission time will also be extended by the timescale for electron cooling. As can be seen from Fig. 4, at low densities the flux is weak and the blast wave hardly decelerates. For most purposes, such interactions can be neglected as they extract only a small amount of energy from that solid angle element of the blast wave. With increasing n_{cl} , the νF_ν flux increases until the cloud density becomes so thick that the RS becomes relativistic, $\Gamma \ll \Gamma_0$, and the emission is received at lower photon energies. At such high densities, the flux received by a distant observer is weak but may last for a long time, especially at small photon energies.

The model light curves show a sharp rise followed by a more leisurely power-law temporal decay. Some of this rapid rise has to do with the idealized cloud geometry: the use of an actual spherical cloud geometry (which could be mimicked by superposition of interacting annuli) would tend to reduce the sharpness in the rising phase of the GRB light curve. As can be seen from the bottom panel of Fig. 4 in a logarithmic representation, the power-law decay of the flux displays a temporal curvature or softening at times well past the peak from cooling breaks in the synchrotron spectrum. This is related to the detection of higher energy photons that were emitted from a higher-energy and usually softer part of the spectrum by off-axis emitting sites (Fenimore et al. 1996; Kumar & Panaiteescu 2000; Dermer 2004; Liang et al. 2006; Zhang et al. 2007). The pulse shapes with $n_{cl} \ll 10^4$ cm $^{-3}$ correspond to kinematic “curvature” pulses (Dermer 2004), where the radiating shell is thin and the emission is radiated promptly on the crossing time defined by the comoving shell thickness, and the spectrum is well described by a single power law in the weak cooling regime. The GRB light curve produced by interactions with such clouds with optimal density $n_{cl} \cong 10^3 - 10^5$ cm $^{-3}$ would represent a generic long-duration GRB except that it is rather weak, reaching peak νF_ν fluxes of $\sim 1 - 2 \times 10^{-8}$ ergs cm $^{-2}$ s $^{-1}$ at ~ 500 keV.⁴

The weakness of the flux is largely due to the small value used for the ϵ_B parameter. Fig. 5 shows the νF_ν SEDs calculated near the peak of the $\epsilon = 1$ light curve at observer time $t = 4.46$ s, for three different cases of ϵ_B and with $n_{cl} = 10^3$ cm $^{-3}$. Other parameters of the event are the same as in Fig. 4. The various components making up the spectrum are shown. The DS component during Phase 2 makes the dominant contribution

⁴ The νF_ν peak flux measured by a GRB telescope integrating over a finite bandwidth would be a factor of a few larger due to a bolometric spectral correction.

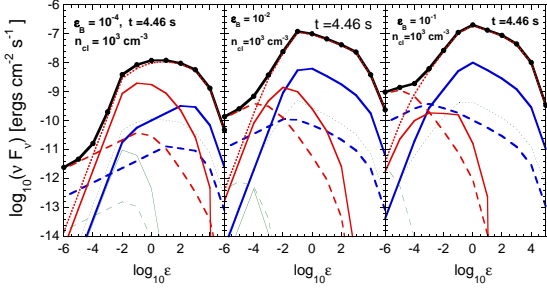


FIG. 5.— Separate spectral components and the total νF_ν flux observed at $\epsilon = 1$ and at 4.46 s after the start of the GRB, near the peak flux of its lightcurve. This GRB pulse model uses parameters given in Table 1, with $n_{cl} = 10^3 \text{ cm}^{-3}$ and $\eta = 1/\Gamma_0$. The differences between the system are that, from left to right, $\epsilon_B = 10^{-4}$, $\epsilon_B = 10^{-2}$, and $\epsilon_B = 0.1$. The total spectrum is given by the heavy solid curve with data points, the FS components are given by the solid curves, the RS components by the dashed curves, and the DS components by the dotted curves. The heavy blue, medium red, and light green curves correspond to Phases 1, 2 and 3, respectively.

to the νF_ν spectra near peak energy release. For the higher magnetic field case $\epsilon_B = 0.01$, and even more so for $\epsilon_B = 0.1$, the stronger cooling causes the Collision Phase components to decay away more rapidly.

For the case $\epsilon_B = 10^{-4}$ on the left, one sees that the peak νF_ν flux, which is important for triggering, is at the level of a few $\times 10^{-8} \text{ ergs cm}^{-2} \text{ s}^{-1}$. BATSE triggered between $\epsilon = 0.1 - \epsilon = 0.6$ at a typical νF_ν flux level of $\approx 5 \times 10^{-8} - 10^{-7} \text{ ergs cm}^{-2} \text{ s}^{-1}$, so such a GRB would be hard to detect unless it occurred nearby ($z \lesssim 1$) and happened to be pointed at us. This cannot be excluded for GRBs without redshift measurements, so our interest for spectral modeling is principally on GRBs that have redshift information. Stronger magnetic fields produce brighter pulses, and when $\epsilon_B \gtrsim 0.01$, the model pulse flux is at the level $\gtrsim 3 \times 10^{-7} \text{ ergs cm}^{-2} \text{ s}^{-1}$, making it an easily detectable GRB with BATSE at $z \cong 1$, and even more so when $\epsilon_B \gtrsim 0.1$ and $\epsilon_e \gtrsim 0.1$, although the adiabatic assumption for the deceleration shock may then become invalid, a situation that can also arise even when $\epsilon_e \sim 0.1$ if photohadronic energy losses are strong (Dermer 2007).

An interesting result of these calculations is that the spectral index below the νF_ν peak is very hard, in number index harder than -0.7 , -1 , and $-4/3$ for $\epsilon_B = 10^{-4}, 10^{-2}$, and 10^{-1} , respectively. In no case does a well-defined cooling spectrum with number index $-3/2$ or softer form. This suggests another argument against the concerns of Ghisellini et al. (2000) that radiative cooling spectra should be observed in GRB spectra. Here there is not sufficient time until the interaction is over for the electrons to cool, so the spectra remain much harder than a cooling synchrotron spectrum below E_{pk} . What stops the interaction and cooling is simply that, after both shocks have passed through the shell and cloud, the disturbed material rapidly expands, shutting off the subsequent synchrotron emissions as nonradiative adiabatic losses increase and the magnetic field intensity, and therefore the synchrotron losses, decrease.

The spectra formed by the interaction of a relativis-

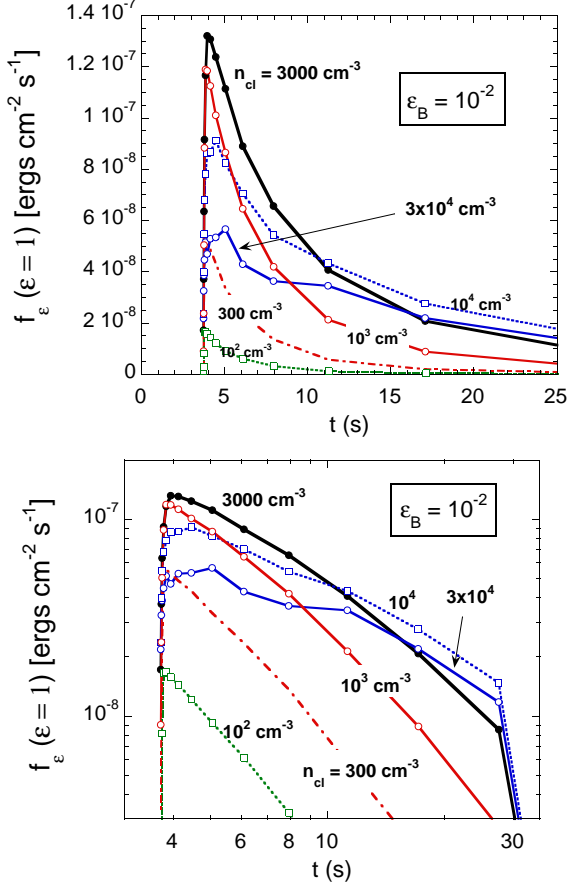


FIG. 6.— Light curves at $\epsilon = 1$ ($h\nu = 511 \text{ keV}$) from the interaction of a GRB blast wave with a cloud for standard GRB pulse model with $\epsilon_B = 10^{-2}$, $\eta = 1/\Gamma_0$, and other parameters given in Table 1, for different values of n_{cl} . Top panel: linear scale. Bottom panel: logarithmic scale.

tic blast wave with a small cloud consisting of both FS and RS emission have the characteristic “Band”-shape (Band et al. 1993), except for a lower energy emission component from the RSs. The relative importance of the RS and FS components increases with increasing ϵ_B for systems with nonrelativistic or weakly relativistic RS. When $\epsilon_B \gg 10^{-4}$, the RS produces a strong optical flux. Indeed, this is the external-shock model explanation for prompt optical emission in GRB emission, first discovered by Akerlof et al. (1999).

Even when $\epsilon_B = 10^{-4}$, the RS emission produces concavity in the X-ray spectrum that could be detectable in joint spectral fitting of the Swift BAT and XRT data with optical/UV measurements with the UVOT and ground-based robotic optical telescopes. For GRBs as modeled by Fig. 5, optical flashes as bright as $m_V \approx 10 - 17$ would be coincident with GRB pulses. The relative amplitude of the reverse shock component is also, however, very sensitive to the value of the shock thickness parameter η , and various underlying assumptions for the constancy of the ϵ_e and ϵ_B parameters with time and equality in the reverse and forward shocks. The rich parameter space could allow detailed modeling of prompt and early afterglow optical light curves from, e.g., RAPTOR, ROTSE, and super-LOTIS.

Fig. 6 shows 511 keV light curves calculated for the standard GRB pulse parameter set with $\epsilon_B = 10^{-2}$,

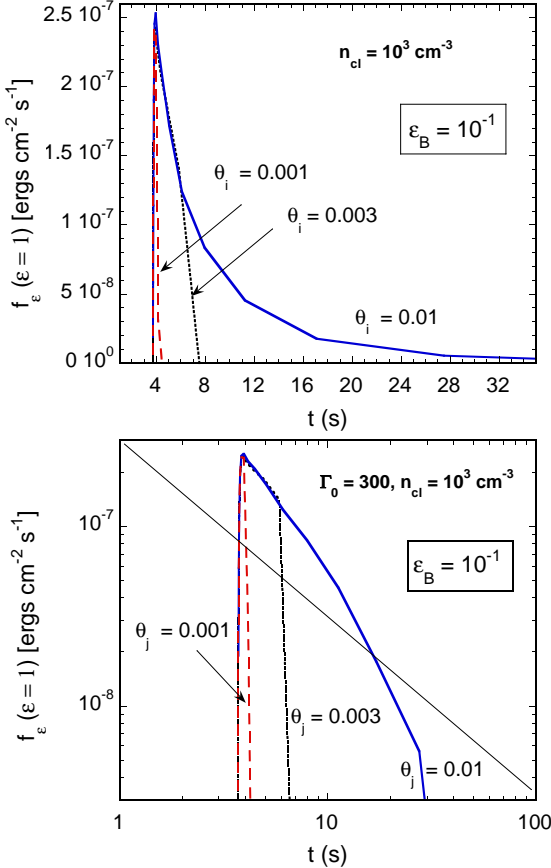


FIG. 7.— Calculated light curves at $\epsilon = 1$ ($h\nu = 511$ keV) from a GRB blast wave impacting a cloud with opening half-angle $\theta_{cl} = 0.01$ located on the symmetry axis of the jet and the line-of-sight to the observer. Parameters for the standard GRB pulse model given in Table 1 are used, with $\epsilon_B = 0.1$ and $\eta = 1/\Gamma_0$. The extent of the jet opening angle is $\theta_j = 0.01, 0.003$, and 0.001 , as labeled. Top panel: linear scale. Bottom panel: logarithmic scale. The straight line is $\propto t^{-1}$.

while varying the cloud density n_{cl} . The same basic behavior as was found in Fig. 4 is apparent, except that the pulse is much brighter and decays more rapidly. The optimal cloud density to make the brightest possible pulse is again near $n_{cl} \cong 10^3 \text{ cm}^{-3}$ for $\epsilon_B = 10^{-2}$ (see Section 4.2). The generic pulse profile found here is typical of a “FRED”-type GRB.⁵ Such a profile could just as easily be produced by a GRB blast wave decelerating in a uniform surrounding medium (Dermer et al. 1999). The external shock model can explain relatively smooth light curves that moreover show various widths and asymmetries. The central question for GRB pulse modeling is, however, whether the rapid variability found in some GRB light curves can be reproduced in an external shock model.

Fig. 7 displays the light curve formed for the standard parameter set with $\epsilon_B = 10^{-1}$ and $\eta = 1/\Gamma_0$. Here the cloud has extent $\theta_{cl} = 0.01$, and a jet with opening half-angle θ_j collides with the cloud. This plot indicates the latitudes from which the pulse flux originates. The high-latitude emission arrives at late times, and most of the fluence is formed by interactions for jet interactions within the Doppler opening angle $1/\Gamma_0$. Although this

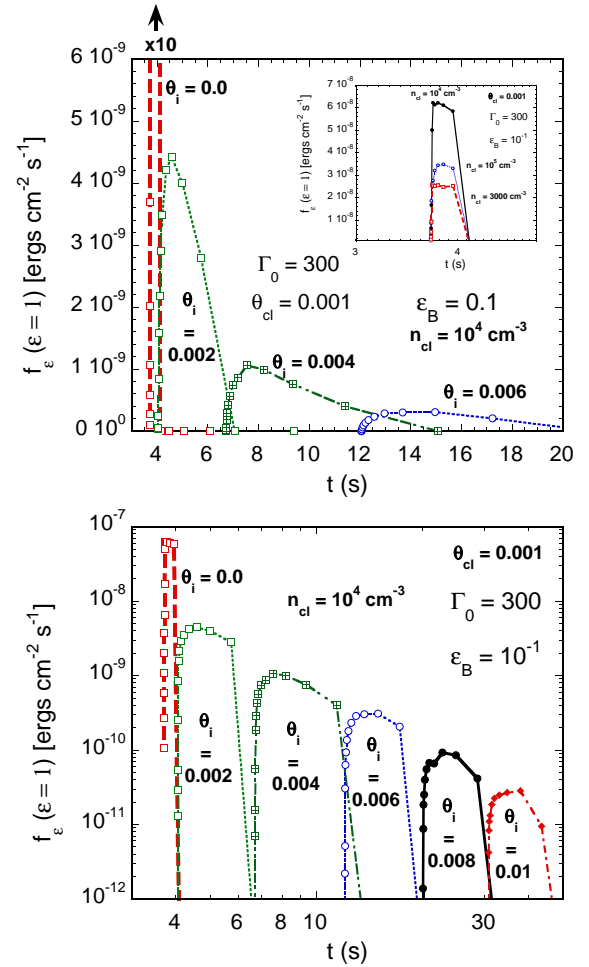


FIG. 8.— Pulses formed by GRB blast wave shells with $\eta = 1/\Gamma_0$ colliding with clouds at different inclinations from the line of sight. The clouds have half-opening angle $\theta_{cl} = 0.001$ which, for $\Gamma_0 = 300$, represents an angular extent equal to $1/3$ of the Doppler cone. Top panel: linear scale. Inset shows detail of brightest pulse. Bottom panel: logarithmic scale.

calculation illustrates the part of the blast-wave/cloud interaction from where the flux originates, the opposite limit, where $\theta_j \gg \theta_{cl}$, is of more interest for producing STV in GRB light curves.

Fig. 8 shows the emission profiles produced by clouds with density $n_{cl} = 10^4 \text{ cm}^{-3}$ and typical sizes $\Delta_{cl} = 0.001 \times x_0 = 0.3x_0/\Gamma_0 = 10^{13} \text{ cm}$, so that their angular extent is smaller than the Doppler angle. The blast wave is assumed to form a thin shell with $\eta = 1/\Gamma_0$. In an idealized circumburst medium where cloud properties were roughly the same throughout this region, then for every bright pulse or two, there would be another ~ 7 dimmer by a factor of $10 - 20$, and another 20 pulses dimmer than the brightest pulse by a factor ≈ 100 . Pulse widths of a second or so are formed by the brightest pulses for such clouds, in keeping with the pulse paradigm (Norris et al. 1996). At late times and from larger angles a lower fluence emission plateau would be formed if the jet and clouds are assumed to maintain roughly uniform properties at these angles.

Because of the unknown distribution of cloud densities, sizes and locations, as well as effects of GRB jet structure, simulating GRB light curves within an external shock scenario is very model-dependent. But simu-

⁵ FRED stands for Fast Rise, Exponential Decay, though the decay phase is often better fit by a power law.

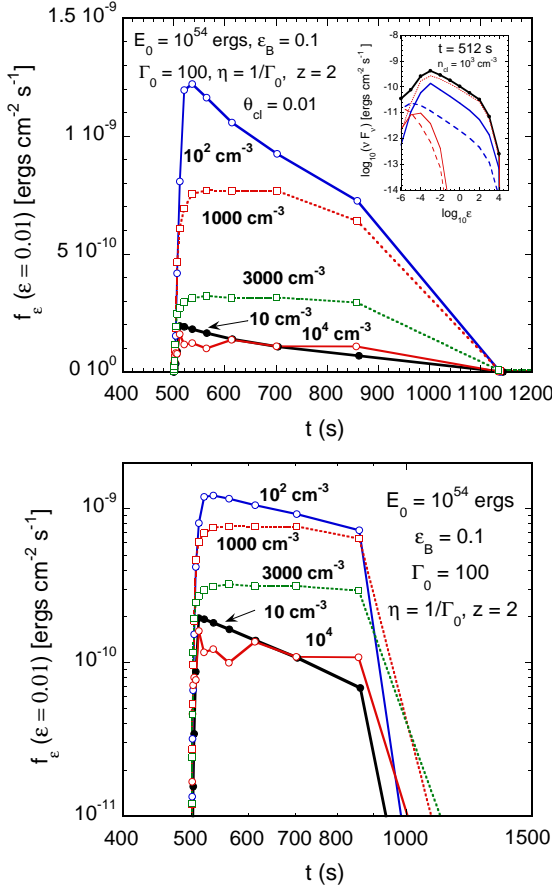


FIG. 9.— Light curves and the SED near the peak of the flare, for emission from a blast-wave shell in the thin-shell approximation $\eta = 1/\Gamma_0$ for a blast-wave Lorentz factor $\Gamma_0 = 100$ impacting an on-axis stationary cloud with opening angle $\theta_{cl} = 0.01$. Top panel: linear flare profiles as a function of n_{cl} . Inset: SED measured at observer time of 512 s and $n_{cl} = 10^3 \text{ cm}^{-3}$ are used. Bottom panel: logarithmic flare profiles as a function of n_{cl} at $\epsilon = 0.01$ ($\approx 5 \text{ keV}$).

lations of GRB light curves with small clouds randomly distributed in a shell show many of the features of spiky GRB light curves (Dermer & Mitman 1999, 2004, and below, Section 4.5).

The calculations shown here mean that given the thin-shell approximation $\eta \cong 1/\Gamma_0$, essentially all BATSE GRBs without redshift information, and many BATSE/Beppo-SAX/HETE-2 GRBs with redshift information can be modeled within an external shock scenario. The standard jet properties are $E_0 = 10^{53} \text{ ergs}$ and $z = 1$, in accord with pre-Swift observations of GRBs with redshift information (Friedman & Bloom 2005). These pulses have SEDs in agreement with BATSE observations (e.g. Preece et al. 2000), bearing in mind different ways to remedy the “line-of-death” problem (Preece et al. 1998) in a nonthermal synchrotron-shock model through the jitter mechanism (Medvedev 2000), radiation reprocessing (Dermer & Böttcher 2000), etc. (see Zhang & Mészáros 2002, for a discussion of GRB spectral break models).

Many X-ray flares observed with Swift can also be modeled within the thin-shell approximation, as illustrated by the calculation shown in Fig. 9. Here the standard X-ray flare parameters from Table 1 are used. The principal difference between these parameters, which apply to Swift observations, and those for the BATSE GRB

pulse observations is that the source redshift is $z = 2$ and the apparent isotropic energy release is 10^{54} ergs , as implied by observations of GRBs at such redshifts (Ghirlanda 2007). The flares were detected by the XRT on Swift, so that the mean telescope photon energy is $\epsilon \lesssim 0.01$. As can be seen, flares at flux levels reaching $10^{-9} \text{ ergs cm}^{-2} \text{ s}^{-1}$ can be made by external shocks. Comparison with observations of GRBs with measured redshifts in the Swift catalog (O’Brien et al. 2006) shows that most flares are well below this level, except for a flare from GRB 050820A at $z = 2.612$ that reached a νF_ν flux between 0.3 and 10 keV of $\approx 10^{-8} \text{ ergs cm}^{-2}$ between 200 and 300 s after the GRB.

The SED for the model GRB X-ray flare peaking hundreds of seconds after the start of the GRB is shown by the inset in Fig. 9. In these flares the reverse-shock synchrotron component can make an enhanced optical/IR emission component due to the concavity produced by the various RS components.

GRBs which lack redshift information, such as GRB 050502B with its enormous X-ray flare exceeding $10^{-9} \text{ ergs cm}^{-2}$ (Falcone et al. 2006a), pose no difficulty to the external shock model.⁶ If the frozen pulse assumption is allowed, then there is no difficulty in explaining γ -ray pulses or X-ray flares in GRBs, provided that the surrounding medium of a GRB is clumpy on well-defined density and size scales.

4. PHYSICS OF PULSE AND FLARE FORMATION IN THE EXTERNAL SHOCK MODEL

We find from this analysis that short pulses or flares can be made if the GRB blast wave undergoes no transverse spreading and interacts with small dense ($\sim 10^3 \text{ cm}^{-3}$) clouds within $\approx 10^{16} - 10^{17} \text{ cm}$ from the GRB explosion. The formation of strong forward shocks with $\Gamma \cong \Gamma_0$ is necessary to make bright pulses, and was the underlying assumption of the GRB light curve simulations in Dermer & Mitman (1999, 2004), where GRB light curves similar to actual GRB light curves were simulated with $\sim 10\%$ efficiency. The implications and plausibility of the assumption of a thin blast wave shell are now considered.

4.1. Temporal Behavior

The characteristic timescales shown in the preceding figures can be understood from simple considerations (Fenimore et al. 1996; Sari & Piran 1997; Dermer & Mitman 1999; Ioka et al. 2005). Eq. (9) gives the time

$$t = \frac{(1+z)x}{\beta_0 c} (1 - \beta_0 \mu_i), \quad (51)$$

since the start of the GRB explosion when emission is first received from a cloud at location x and inclination angle $\theta_i = \arccos \mu_i$ that is impacted by a blast wave moving with Lorentz factor Γ_0 . The angular timescale giving the temporal duration over which emission, emitted at radius x in the angular range $\theta_2 = \theta_i + \theta_{cl} > \theta_1 = \max(0, \theta_i - \theta_{cl})$, is received is simply

$$\frac{\Delta t^{ang}}{1+z} = \frac{x}{\beta_0 c} (\mu_1 - \mu_2) \xrightarrow{\theta_1, \theta_2 \ll 1, \Gamma_0 \gg 1} \cong$$

⁶ Because the νF_ν peak flux was above the Swift BAT energy window, the fraction of total GRB fluence in the X-ray flare is unknown.

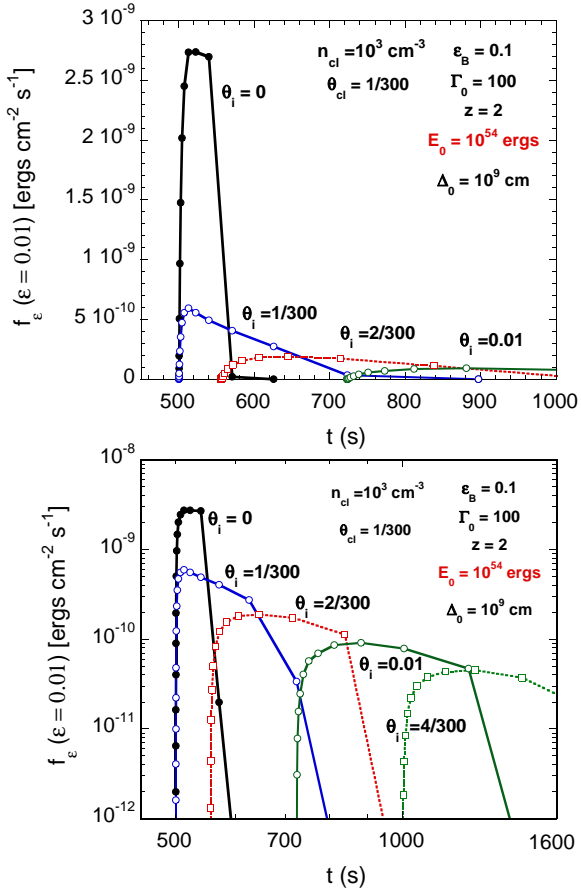


FIG. 10.— Light curves of emission from a blast-wave shell/stationary cloud interaction in the frozen-pulse approximation $\eta \rightarrow 0$ for a blast-wave Lorentz factor $\Gamma_0 = 300$ impacting an on-axis cloud with opening angle $\theta_{cl} = 1/300$ and $\Delta_0 = 10^9$ cm. Top panel: linear flare profiles as a function of incidence angle θ_i for $n_{cl} = 10^3$ cm $^{-3}$ at $\epsilon = 0.01$. Bottom panel: logarithmic flare profiles.

$$\frac{x}{2c} (\theta_2^2 - \theta_1^2) \cong \left(\frac{x}{2c} \right) 4\theta_i \theta_{cl} \quad (52)$$

when $\theta_i > \theta_{cl}$, and

$$\frac{\Delta t^{ang}}{1+z} \cong \frac{x}{2c} (\theta_i^2 - \theta_{cl}^2) \quad (53)$$

when $\theta_i < \theta_{cl}$.

The radial timescale for emission from two points at different distances x_1 and x_2 but at the same inclination angle θ_i is given from eq. (20) by

$$\frac{\Delta t^{rad}}{1+z} = \frac{\Delta_{cl}}{\beta_0 c} (1 - \beta_0 \mu_i) \cong t_{z0} \left(\frac{\Delta_{cl}}{x} \right) (1 + \theta_i^2 \Gamma_0^2). \quad (54)$$

We define the on-axis observer collision time

$$t_{z0} \equiv \frac{(1+z)x}{2\Gamma_0^2 c}, \quad (55)$$

and the inclination and cloud angles in units of the Doppler angle $\theta_0 = 1/\Gamma_0$ by the relations

$$v_i = \Gamma_0 \theta_i \text{ and } v_{cl} = \theta_{cl} \Gamma_0,$$

respectively. The characteristic duration of a shell/cloud collision is therefore

$$\Delta t \cong t_{z0} \max \left[\frac{2v_{cl}}{1+v_i^2} (1+v_i^2), \frac{2v_{cl}}{1+v_i^2} \right],$$

$$4v_i v_{cl} H(v_i - v_{cl}) + (v_i + v_{cl})^2 H(v_{cl} - v_i) \right], \quad (56)$$

where $H(u) = 1$ if $u \geq 1$ and $H(u) = 0$ otherwise. Note that the angular timescale is independent of cloud location x , using $v_{cl} = \Gamma_0 \theta_{cl} = (\Delta_{cl}/x) \Gamma_0$ in eq. (56), but depends on cloud size Δ_{cl} and inclination angle θ_i . The radial timescale is also independent of x when written in terms of cloud size.

The STV condition for the external shock model is $v_{cl} \ll 1$. Thus we see that the kinematic duration is determined by the angular timescale everywhere except when $v_i \leq 1/2\Gamma_0$, that is, for nearly on-axis clouds with $\theta_i \leq 1/2\Gamma_0^2$. The kinematic duration of the pulse $\Delta t \propto 1/\theta_i$ for $\theta_i \geq 1/2\Gamma_0^2$. The pulse shortening for nearly on-axis events, combined with beaming factors and spectral effects, is shown from analyses and Monte Carlo simulations capable of explaining the range of observed GRB BATSE light curves (Dermer & Mitman 1999, 2004).

4.2. Optimal Cloud Density for Bright Pulses

The optimal density giving the brightest measured flux can be derived from three requirements:

1. A strong FS which, from eq. (13), implies a maximum cloud density given by

$$n_{cl} \lesssim \frac{E_0}{16\pi x^2 \Gamma_0^4 m_p c^2 \Delta(x)}. \quad (57)$$

2. Significant blast-wave deceleration to provide efficient energy extraction, which requires clouds with thick columns (Dermer & Mitman 1999), that is, with densities

$$n_{cl} \gtrsim \frac{E_0}{4\pi x^2 \Gamma_0^2 m_p c^2 \Delta_{cl}}. \quad (58)$$

3. The requirement of a strong FS and a thick column therefore translates into the requirement that

$$\Delta_{cl} \gtrsim 4\Gamma_0^2 \Delta(x) \quad (59)$$

in order to produce STV. The STV condition is

$$\theta_{cl} = \frac{\Delta_{cl}}{x} = \frac{v_{cl}}{\Gamma_0} \ll \frac{1}{\Gamma_0}. \quad (60)$$

Using eq. (2) for the shell width, eq. (59) becomes

$$4\eta\Gamma_0 < \frac{4\Gamma_0^3 \Delta_0}{x} + 4\eta\Gamma_0 \ll 1,$$

so that the requirement on the width of the radiating shell material in the external shock model for rapid variability is simply that

$$\eta \lesssim \frac{1}{4\Gamma_0} \text{ when } x \gtrsim 4\Gamma_0^3 \Delta_0 \cong 10^{15} \Gamma_{300}^3 \Delta_7 \text{ cm}. \quad (61)$$

It is therefore not possible to have STV if $\eta \cong 1$, because then the reverse shock is relativistic, the forward shock Lorentz factor is low and Doppler boosting is lost. But it becomes possible in the thin-shell approximation $\eta \sim 1/\Gamma_0$. As shown by the light curves and SED calculations, the phenomenology of GRBs can be explained in the frozen pulse ($\eta = 0$) and also, possibly, the thin-shell approximation.

The optimal cloud density for bright variable pulses in the external shock model, from eq. (57) for a GRB blast wave with apparent isotropic energy release $E_0 = 10^{54}E_{54}$ ergs and shell width $\Delta(x) = 10^7\Delta_7$ cm that encounters a cloud at $10^{16}x_{16}$ cm from the center of the GRB explosion, is

$$n_{cl}(\text{cm}^{-3}) \approx 1.6 \times 10^6 \frac{E_{54}}{x_{16}^2 \Gamma_{300}^2 \Delta_7}. \quad (62)$$

For instance, the calculations shown in Fig. 5 with $\eta = 1/\Gamma_0$ have $\Delta_7(x = 10^{16} \text{ cm}) = 38$.

4.3. Width of Radiating Shell

Besides the requirement for STV that the unshocked fluid shell be thin or frozen, the width of the shocked fluid shell cannot be too great, for otherwise rapid variability would be washed-out by contributions from different parts of the shell.

First consider a blast wave sweeping up matter from a uniform surrounding circumburst medium with density $n_0(\text{cm}^{-3})$. The swept-up material, compressed by the factor 4Γ at the external shock, has thickness

$$\Delta'_{sh}(x) = \frac{x}{12\Gamma} \quad \text{and} \quad \Delta_{sh}(x) = \frac{x}{12\Gamma^2} \quad (63)$$

in the proper and explosion frames, respectively. Because the angular extent of the shocked fluid layer in the blast wave covers the full Doppler cone, the variability is already limited to a timescale $\gtrsim 0.25t_{z0}$ by light travel time limitations. Under these circumstances, rapid variability is not expected, even when considering density jumps (Nakar & Granot 2006).

Now consider the transverse width of the shocked fluid shell colliding with a cloud with Dopper size $v_{cl} \ll 1$ that subtends the solid angle $\Delta\Omega_{cl}$ as seen from the center of the explosion. By equating the mass $m_p \Delta\Omega_{cl} x^2 n'(x) \Delta'_{sh}(x)$ with the cloud mass $m_p \Delta\Omega_{cl} x^2 n_{cl} \Delta_{cl}$ we have, using the relativistic density jump condition $n'(x) = 4\Gamma n_0$,

$$\Delta'_{sh}(x) = \frac{\Delta_{cl}}{4\Gamma} = \frac{v_{cl}x}{4\Gamma^2} \quad \text{and} \quad \Delta_{sh}(x) = \frac{v_{cl}x}{4\Gamma^3}, \quad (64)$$

i.e., a shocked-fluid layer thinner than required to produce STV.

4.4. Thin Shell Assumption

From the preceding discussion, one can see that the viability of an external shock model for the γ -ray pulses and X-ray flares depends on whether the GRB blast-wave width spreads in the coasting phase according to eq. (2), with $\eta \lesssim 1/\Gamma_0$. In the gas-dynamical study of Mészáros et al. (1993), inhomogeneities in the GRB fireball produce a spread in particle velocities of order $|v - c|/c \sim \Gamma_0^{-2}$, so that $\Delta(x) \sim x/\Gamma_0^2$ when $x \gtrsim \Gamma_0^2 \Delta_0$ and $\eta \sim 1$. This expression was also obtained in the hydrodynamical analysis by Piran et al. (1993).

Several points can be made about these results. First, gas-dynamical or hydrodynamic analyses omit the fluid nature of the explosion plasma whose behavior depends crucially on the the magnetic field and MHD properties of the fluid. Second, the spread in Δ considered for a spherical fireball is averaged over all directions. As the fireball expands and becomes transparent, the variation

in fluid motions or gas particle directions over a small solid angle $\sim 1/\Gamma_0^2$ of the full sky becomes substantially less. Small values of η could be realized if there is little dispersion in the baryon-loading of the fluid shell within the small range of solid angles subtended by the jet from which the observed emission is radiated. Third, the particles within the cold unshocked blast-wave shell will expand and adiabatically cool so that the fluid will spread with thermal speed $v_{th} = \beta_{th}c$. The comoving width of the blast wave is $\Gamma_0 \Delta_0 + \beta_{th} c \Delta t' \approx \Gamma_0 \Delta_0 + \beta_{th} x/\Gamma_0$, so that the spreading radius $x_{spr} \cong \Gamma_0^2 \Delta_0 / \beta_{th}$. Adiabatic expansion of nonrelativistic particles can produce a very cold shell with $\beta_0 \lesssim 10^{-3}$, leading to very small shell widths.

The requirement on the thinness of $\Delta(x)$ does not apply to the adiabatic self-similar phase, where the width of the shocked fluid shell is $\Delta_{sh} \sim x/12\Gamma_0^2$, as implied by the relativistic shock jump equations (Blandford & McKee 1976); see eq. (63). Consequently, no extreme variability is expected when a blast wave, already in the adiabatic self-similar regime, encounters a density jump, as demonstrated by Nakar & Granot (2006) (in agreement with the results of unpublished numerical simulations using the code described by Chiang & Dermer (1999)). But even in this case, however, $\Delta \ll x/\Gamma_0^2$ if the blast wave is highly radiative (Cohen et al. 1998), which could result from leptonic processes when $\epsilon_e, \epsilon_B \gtrsim 0.1$, or hadronic processes when $\epsilon_e \sim 0.1$ and $\epsilon_B \gtrsim 0.1$ and the surrounding circumburst medium is dense, with $n_0 \gtrsim 10^3 \text{ cm}^{-3}$ (Dermer 2007).

This question deserves considerably more study, and will require at least an MHD model employing self-consistent particle distributions and magnetic field geometries in the erupting plasma, generation and amplification of the magnetic field in the shocked fluid layer (including particle acceleration and diffusion into the cold fluid shell), and magnetic field and particle energy evolution from shell expansion.

4.5. Simulations of GRB Light Curves

Fig. 11 shows Monte Carlo simulations, described in more detail in Dermer & Mitman (2004), of GRB light curves under the assumption that the cold blast wave shell remains thin and the interaction forms a strong forward shock. The parameters of the simulation are shown in Table 2, and here we use fixed cloud sizes with radius r_1 that are “uniformly randomly” distributed in the volume between R_1 and R_2 . In all cases, the surface filling factor $\xi = 10\%$, and a fraction $\zeta = 10\%$ of the blast wave energy intercepted by the cloud is transformed into radiation received by the detector at energy $m_e c^2 \epsilon$. The angular extent of the jet is k_θ/Γ_0 , and an occulting factor is included so that the portion of the blast wave that intercepts a cloud at a smaller radius no longer radiates when interacting with clouds at larger radii.

The top four panels represent the GRB prompt phase detected near 100 keV using parameters appropriate to BATSE, including noise at a level typical of the BATSE detectors. The bottom two panels make use of parameters that would apply to Swift. The variety of simulated light curves is endless, depending on the seed used in the random number generator and the choices of cloud and blast wave parameters. Precursor events can be made if some material is found very close to the GRB (Piro et

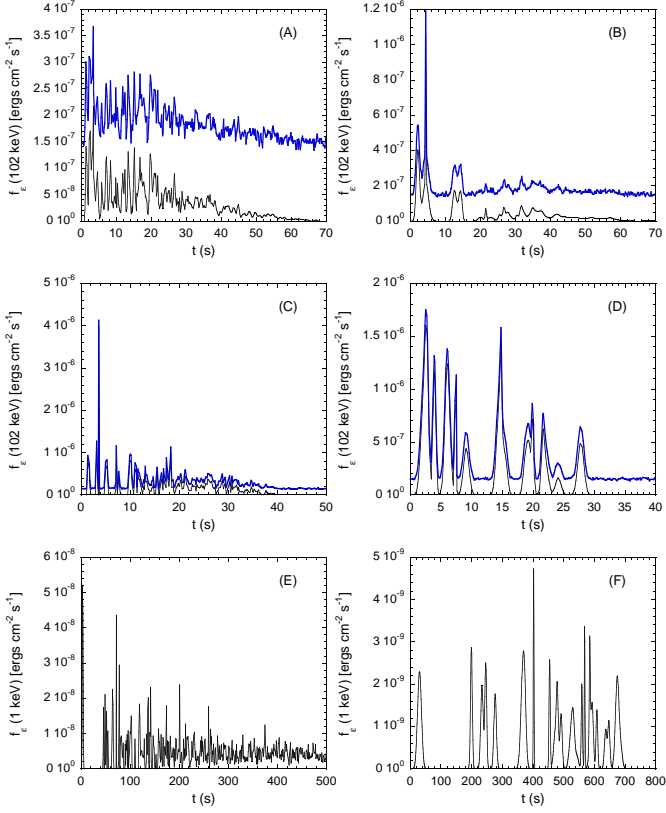


FIG. 11.— Simulated GRB lightcurves from the interaction of a thin blast wave with clouds with thick columns, using parameters from Table 2. In the top four panels, the lower curve is the GRB emission, and the upper curve is this emission added to a Gaussian noise typical of BATSE detectors.

al. 2005, compare panel E).

4.6. Criticisms of the External Shock Model

We describe the general criticisms that the external shock model for prompt GRB emissions has endured. Fenimore et al. (1996) demonstrated that an expanding blast wave would, if briefly illuminated over a large portion of its surface covering the Doppler cone, make progressively longer pulses in accordance with the relation $t \cong (1+z)x/\Gamma^2 c$. The tendency for pulse lengthening can be avoided if a small fraction of the blast wave surface area within the Doppler cone were illuminated at any one time, but this was thought to require an unreasonable number of illuminating regions (“clouds”).

One approach is to estimate a maximum “surface filling factor” of radiating sites consistent with measured variability, using kinematic arguments (Fenimore et al. 1999). Sari & Piran (1997) argued that highly variable light curves cannot be constructed from blast-wave interactions with surrounding density inhomogeneities by superposing pulses made near the outer region of the Doppler cone to show how they overlap due to the large angular timescales; hence the sources of GRBs must require an active central engine to make discrete pulses. Dermer & Mitman (2004) showed that this argument, made also more recently by Piran (2005) and Ioka et al. (2005), mistakenly uses the angular time scale near the outer edge of the Doppler cone, and misses a number of important points: One is that the beaming factors, not considered in these papers, heavily weight the total

fluence for near on-axis clouds, and even more so the pulse peak flux because of the smaller kinematic variability timescale for nearly on-axis clouds; another is the different (observer) times for the clouds nearly on-axis as compared with those off-axis, so that flux ratios from different parts of the shell are time-dependent; a third is the assumption that clouds are distributed with azimuthal symmetry within the Doppler cone; a fourth is that the beaming factor of the relativistic jet that forms γ -ray pulses in the prompt phase may be smaller than $\sim \Gamma_0^{-1}$ and the typical angles inferred from optical afterglow breaks, which will reduce the importance of off-axis events. The crucial role of the narrow cold blast-wave fluid shell (not the shocked fluid shell considered by Nakar & Granot (2006)) to ensure a strong forward shock has also been overlooked in past studies.

Ramirez-Ruiz & Fenimore (2000) claim that the lack of pulse-width evolution in BATSE GRB light curves favors internal shock models; Kocevski et al. (2007), in the absence of any quantitative consideration of external shocks, argue that XRT pulse spreading in Swift GRBs favors internal shock models. From our simulations, we see that this effect is subtle at best in the unlikely condition when the clouds are “uniformly randomly” situated. Realistic cloud clustering properties or a narrow γ -ray jet could obscure this effect completely. Lazzati & Perna (2007) derive the time-scale ratio $\Delta t_v/\bar{t} \sim 0.25$ for a spherical shell and suggest that the observational data indicate a clustering in the value $\Delta t_v/\bar{t} \sim 0.25$ that rules out the external shock model, but nowhere consider observational biases for the detection of flare profiles with larger or smaller time-scale ratios, or whether this time-scale ratio could reflect cloud properties.

As shown in the simulations, STV in the external shock model with moderate ($\sim 10\%$) efficiency is possible if the blast wave interacts with clouds with thick columns and sizes $\Delta_{cl} \ll x/\Gamma_0$, because then the condition of “local spherical symmetry” (Fenimore et al. 1996) is broken. The shortest pulses carrying a significant fraction of the total fluence are made by interactions of the blast wave with small clouds at angles $\theta \ll 1/\Gamma_0$ to the observer line-of-sight (Dermer & Mitman 2004). Efficiency concerns are reduced if the fraction of energy dissipated as X-rays and γ rays is a small fraction of the total (Dermer 2007).

5. DISCUSSION

We have critically examined whether external shock processes can make short timescale X-ray and γ ray variability in the γ -ray luminous phase and the early afterglow phase, extending to $\gtrsim 10^4$ s after a GRB trigger. The result is simple: external shocks can only make the erratic variability observed in GRB light curves if the cold fluid shell ejected by the impulsive burst event does not spread significantly from its initial characteristic width $\Delta t_{exp}/c$ at the time of the GRB explosion, where Δt_{exp} , assumed to be $\ll 1$ s, is the time of the energy release in the explosion frame. The question of whether lack of shell spreading is a valid assumption, at least within the Doppler cone primarily sampled by the observer, is an open question but plausibly valid. A crucial point is that an external shock model for the rapid variability is feasible because the GRB blast wave is still in its coasting phase, and has not yet reached the adiabatic self-similar phase.

Let us follow the implications if this assumption were allowed.

One way to interpret GRB light curve data is to suppose that there is a single impulsive burst of energy, and all subsequent phenomenology is a consequence of the collimated ultra-relativistic blast wave interacting with its surroundings (Mészáros & Rees 1993; Dermer & Mitman 1999, 2004). External shocks are the basis for the success that the relativistic blast-wave physics model has had in interpreting GRB afterglows (Mészáros & Rees 1997; Zhang & Mészáros 2004); we also suppose that its success can be translated to the prompt phase. The properties of the surrounding medium, as implied by extensive evidence on GRB host galaxy studies, is determined by the type of GRB progenitor, which is a massive ($\gtrsim 10 - 20 M_{\odot}$) star lacking a H envelope whose core collapses to form a Type 1b/c SN. The SNR and the progenitor stellar wind, including effects of a possible binary companion (Fryer et al. 2007), form a complicated surroundings that imprints its structure on the GRB light curves (Dermer & Mitman 1999; Wang & Loeb 2000).

The brief impulsive energy releases in GRB explosions, which for neutrino-mediated processes are most efficient for \simeq ms timescales, are compatible with brief collapse events or phase transitions from stellar cores to compact objects, for example, from neutron star to black hole or neutron star to a quark star (e.g., Drago et al. 2005; Berezhiani et al. 2003). This collapse event would follow by minutes, hours, days or more a Type 1b/c supernova that forms a supramassive, rotationally supported neutron star/magnetar. This picture is a two-step collapse model, like the supranova model of Vietri & Stella (1998, 1999), though with a short delay.

Such a picture, orthogonal in all respects to the collapsar model except for the primary role of high mass stars as long-duration GRB progenitors, has a great deal of explanatory and predictive capability. Here we point out some of the attractive features of such a picture:

1. ^{56}Ni . The direct collapse of the evolved core of a massive star to a black hole in the collapsar model, avoiding core bounce, requires new routes for the production of ^{56}Ni . This makes the similarity between the peak optical rest frame M_V magnitudes (taken as a proxy for ^{56}Ni production) measured in SNe associated with GRBs and Type 1b/c SNe not associated with GRBs (Soderberg et al. 2005) a remarkable coincidence. Two-step collapse processes avoid this coincidence by forming ^{56}Ni through neutron-star core bounce.
2. Energy reservoir. The discovery (Frail et al. 2001; Panaiteescu & Kumar 2001; Friedman & Bloom 2005) of a standard energy reservoir, or at least a clustering of beaming-corrected absolute energies towards a value $\cong 10^{51}$ ergs, modulo an uncertain efficiency to convert explosion energy into γ rays, fixes the energy budget of the GRB explosion. The collapse of a rotationally-supported neutron star to a black hole, or the transition from a degenerate neutron fluid to quark state, could liberate kinetic energies approaching a constant maximum energy that may not defy ability or require excessive assumptions to calculate. If the explosion involves a neutrino or Poynting-flux mediated inter-

action, values of collimated electromagnetic energy of $\approx 10^{51} - 10^{52}$ ergs could be released in a second collapse to a black hole.

3. Complex circumburst medium. A magnetar phase (Usov 1992) follows, even if only by minutes, the first collapse event, and drives a strong pulsar wind to disrupt, thread, and render extremely complex the surrounding medium. The work of Königl & Granot (2002) shows the profound impact on the circumburst medium that this phase can have for long (month-yr) delays.
4. Clean environment. The Usov phase cleans the environment except for dense clumps formed at distances where the strong radiation pressure can be withstood—and these are the clumps that form the clouds in the external shock model. Close to the explosion trigger, the environment of a rotationally-supported neutron star is baryon-clean (Vietri & Stella 1998).
5. Explanation for chromatic X-ray and optical afterglow beaming breaks. Panaiteescu et al. (2006) compare Swift BAT X-ray light curves with optical light curves taken from a variety of telescopes for 6 GRBs, finding several instances where the X-ray light curves appear to decay chromatically with respect to the optical light curves. Possible explanations for these observations are evolving ϵ_e and ϵ_B parameters and the addition of the (synchrotron self-)Compton for a beamed outflow (illustrated numerically by Dermer et al. 2000), which plausibly explains the light curves of GRB 050922C and the lack of X-ray breaks observed with Swift (Sato et al. 2007). The optical light curves of GRBs 050607, 050802, and 050713A are too poorly sampled to draw definitive conclusions, and the optical and X-ray light curves in GRB 050319 appear to follow each other except for a final high optical datum. This leaves only GRB 050401 to explain. More and better data is clearly needed.
6. Explanation for the decay and plateau phases observed with Swift. Within the context of the external shock model for a GRB taking place within a uniform surrounding environment, I recently showed that an intense photohadronic phase, effectively depleting internal GRB blast wave energy, could cause the X-ray light curves to exhibit rapid flux declines (Dermer 2007). After the discharge, the blast wave regains its nonradiative character to form the plateaus observed with Swift.
7. High energy radiation. Observations of GRBs with the GLAST GBM and LAT will monitor the Compton components in the spectrum of a GRB. Definite correlations between the leptonic synchrotron and SSC components are expected, which behave in stark contrast to photohadronic γ -ray components that vary independently of the lower-energy lepton synchrotron component. GLAST will search for photohadronic emission components and, in conjunction with detectors such as IceCube, test multi-wavelength and multi-channel predictions (Dermer et al. 2007).

8. Predictions. With respect to the short-delay supernova model, the confirming prediction is to glimpse the GRB progenitor in its magnetar phase prior to the second-step collapse to form the GRB. Analysis of radio, optical, X-ray, or γ -ray emissions to obtain $P(t)$ and $\dot{P}(t)$ in the brief interval between the two collapse events is now only possible with broad field-of-view detectors with poor sensitivities. Unfortunately, optical supernova discovery generally happens within a few weeks after the supernova event, by which time a second collapse would have happened. So for the short-delay supernova intervals consistent with the offset between nearby GRBs and their supernova emissions (Zeh et al. 2004), this prediction is not promising except to test the standard supernova model (Vietri & Stella 1998).

A definitive test of the collapsar model is to find a supernova taking place well in advance of the GRB, so that the GRB has no detectable supernova emissions. Development of telescopes with wide field-of-view optical survey capabilities, like Pan-STARRS or SNAP, holds promise to rule out the collapsar model for specific GRBs (C. Dermer & A. Drago, unpublished, 2006), and could also provide a database to search for magnetar activity in advance of a GRB.

6. SUMMARY AND CONCLUSIONS

A detailed analysis of the interaction between a relativistic blast wave and a stationary cloud was performed in the limit that the cloud width $\Delta_{cl} \ll x$, so that the shell density remains effectively constant during the interaction. Synchrotron light curves and spectra from such interactions were calculated for a range of cloud densities, sizes, and locations, for blast-wave coasting

Lorentz factors $\Gamma_0 = 100$ and 300 , and for different blast-wave widths.

In order to produce short timescale variability in the external shock model, the shell width parameter η must be $\lesssim 1/\Gamma_0$, as demonstrated both analytically and numerically. If this model assumption is valid, then the external shock model can explain the generic spectral shape of GRB pulses, rapid variability in GRB light curves observed with BATSE, and the delayed X-ray flares observed with Swift. The tendency of the GRB pulses or X-ray flares to diminish in intensity with time is a consequence of the expansion of the blast wave. The durations of GRB pulses reflect the dimensions of the surrounding thick-columned clouds. The typical distances of the clouds that produce γ -ray pulses are $\approx 10^{15} - 10^{17}$ cm from the GRB explosion center, with cloud sizes $\simeq 10^{12} - 10^{13}$ cm and densities $\sim 10^3$ cm $^{-3}$. The clouds that produce X-ray flares observed with Swift are typically found $\gtrsim 10^{17}$ cm from the center of the GRB explosion, and have sizes $\lesssim 10^{15}$ cm and densities $\sim 10^3$ cm $^{-3}$.

This analysis also provides a basis for making accurate calculations of light curves and spectra formed by both forward and reverse shocks in collisions between relativistic shells.

I would like to thank A. Atoyan, D. Band, M. Böttcher, C. Fryer, M. González, J. Granot, E. Nakar, and E. Ramirez-Ruiz for discussions. I would especially like to thank Kurt Mitman for the use of the numerical simulation code that we developed to study this problem, and Alessandro Drago for his visit. This work was supported by the Office of Naval Research. I gratefully acknowledge GLAST Interdisciplinary Science Investigator grant DPR S-13756G and Swift Guest Investigator grants, without which this research would not be possible.

REFERENCES

Atoyan, A. M., & Dermer, C. D. 2003, ApJ, 586, 79
 Akerlof, C., et al. 1999, Nature, 398, 400
 Bahcall, J. N., & Mészáros, P. 2000, PRL, 85, 1362
 Band, D. L., 2006, ApJ, 644, 378
 Band, D., et al. 1993, ApJ, 413, 281
 Barthelmy, S. D., et al. 2005, ApJ, 635, L133
 Beloborodov, A. M. 2000, ApJ, 539, L25
 Beloborodov, A. M. 2003, ApJ, 585, L19
 Berezhiani, Z., Bombaci, I., Drago, A., Frontera, F., & Lavagno, A. 2003, ApJ, 586, 1250
 Blandford, R. D., & McKee, C. F. 1976, Physics of Fluids, 19, 1130
 Böttcher, M., & Dermer, C. D. 2000, ApJ, 532, 281
 Burrows, D. N., et al. 2005, Science, 309, 1833
 Burrows, D. N., et al., 2005a, X-Ray Universe 2005 conference proceedings, astro-ph/0511039
 Burrows, D. N., et al. 2007, astro-ph/0701046
 Chiang, J., & Dermer, C. D. 1999, ApJ, 512, 699
 Derishev, E. V., Kocharyan, V. V., & Kocharyan, V. V. 1999, ApJ, 521, 640
 Cohen, E., Piran, T., & Sari, R. 1998, ApJ, 509, 717
 Daigne, F., & Mochkovitch, R. 1998, MNRAS, 296, 275
 Dermer, C. D., & Mitman, K. E. 2004, Astronomical Society of the Pacific Conference Series, 312, 301
 Dermer, C. D., Ramirez-Ruiz, E., & Le, T. 2007, PRL, submitted
 Dermer, C. D. 2004, ApJ, 614, 284
 Dermer, C. D., & Böttcher, M. 2000, ApJ, 534, L155
 Dermer, C. D., Chiang, J., & Mitman, K. E. 2000, ApJ, 537, 785
 Dermer, C. D., 2007, ApJ, submitted (astro-ph/0606320)
 Dermer, C. D., Böttcher, M., & Chiang, J. 1999, ApJ, 515, L49
 Dermer, C. D., & Humi, M. 2001, ApJ, 556, 479
 Dermer, C. D., & Mitman, K. E. 1999, ApJ, 513, L5
 Drago, A., Lavagno, A., & Parenti, I. 2005, astro-ph/0512652
 Falcone, A. D., & The Swift XRT Team 2006, AIP Conf. Proc. 836: Gamma-Ray Bursts in the Swift Era, 836, 386
 Falcone, A. D., et al. 2006a, ApJ, 641, 1010
 Fenimore, E. E., Cooper, C., Ramirez-Ruiz, E., Sumner, M. C., Yoshida, A., & Namiki, M. 1999, ApJ, 512, 683
 Fenimore, E. E., Madras, C. D., & Nayakshin, S. 1996, ApJ, 473, 998
 Fishman, G. J. 1999, A&AS, 138, 395
 Frail, D. A., et al. 2001, ApJ, 562, L55
 Friedman, A. S., & Bloom, J. S. 2005, ApJ, 627, 1
 Fryer, C. L., et al. 2007, astro-ph/0702338
 Gehrels, N., et al. 2004, ApJ, 611, 1005
 Ghirlanda, G. 2007, astro-ph/0702212
 Ghirlanda, G., Nava, L., Ghisellini, G., & Firmani, C. 2007, A&A, in press (astro-ph/0702352)
 Ghisellini, G., Celotti, A., & Lazzati, D. 2000, MNRAS, 313, L1
 Granot, J., Piran, T., & Sari, R. 1999, ApJ, 513, 679
 Guetta, D., Spada, M., & Waxman, E. 2001, ApJ, 557, 399
 Guetta, D., & Piran, T. 2006, A&A, 453, 823
 Gupta, S., Böttcher, M., & Dermer, C. D. 2006, ApJ, 644, 409
 Ioka, K., Kobayashi, S., & Zhang, B. 2005, ApJ, 631, 429
 Kobayashi, S., & Sari, R. 2001, ApJ, 551, 934
 Kobayashi, S., Piran, T., & Sari, R. 1999, ApJ, 513, 669
 Kobayashi, S., Piran, T., & Sari, R. 1997, ApJ, 490, 92
 Kocevski, D., Butler, N., & Bloom, J. S. 2007, ApJ, submitted (astro-ph/0702452)
 Königl, A., & Granot, J. 2002, ApJ, 574, 134
 Kumar, P., & Panaiteescu, A. 2000, ApJ, 541, L51

TABLE 1
STANDARD BLAST WAVE AND CLOUD
PARAMETERS^a

	GRB pulse	X-ray Flare
Redshift z	1.0	2.0
$d_L(10^{28} \text{ cm})$	2.02	4.80
E_0 ergs	10^{53}	10^{54}
Γ_0	300	100
Δ_0	10^7 cm	
η	$\Gamma_0^{-1}, 0$	
ϵ_e	0.1	
ϵ_B	$10^{-1}, 10^{-4}$	
ϵ_2	0.1	
p	2.5	
θ_{cl}	0.01	
θ_i	0.0	
$x_0(\text{cm})$	10^{16}	10^{17}
$x_2(\text{cm})$	1.02×10^{16}	1.02×10^{17}
$n_{cl}(\text{cm}^{-3})$	10^3	

^aForward and reverse shock parameters are the same.

Kumar, P. 1999, ApJ, 523, L113
 Lazzati, D., & Perna, R. 2007, MNRAS, 375, L46.
 Le, T., & Dermer, C. D. 2007, ApJ, in press, astro-ph/0610043
 Liang, E., Zhang, B., Virgili, F., & Dai, Z. G. 2006a, ApJ, submitted (astro-ph/0605200)
 Liang, E. W., et al., 2006, ApJ, 646, 351
 Lyutikov, M., & Blackman, E. G. 2001, MNRAS, 321, 177
 Mimica, P., Aloy, M. A., Müller, E., & Brinkmann, W. 2005, A&A, 441, 103
 Medvedev, M. V. 2000, ApJ, 540, 704
 Mészáros, P. 2006, Reports of Progress in Physics, 69, 2259
 Mészáros, P., Laguna, P., & Rees, M. J. 1993, ApJ, 415, 181
 Mészáros, P., & Rees, M. J. 1997, ApJ, 476, 232
 Mészáros, P., & Rees, M. J. 1993, ApJ, 405, 278
 Mimica, P., Aloy, M.-A., & Mueller, E. 2007, A&A, accepted (astro-ph/0611765)
 Nakar, E., & Granot, J. 2006, MNRAS, submitted (astro-ph/0606011)
 Norris, J. P., Nemiroff, R. J., Bonnell, J. T., Scargle, J. D., Kouveliotou, C., Paciesas, W. S., Meegan, C. A., & Fishman, G. J. 1996, ApJ, 459, 393
 O'Brien, P. T., et al., 2006, ApJ, 647, 1213
 O'Brien, P. T., Willingale, R., Osborne, J. P., & Goad, M. R. 2006a, New Journal of Physics, 8, 121
 Panaiteescu, A., Mészáros, P., Burrows, D., Nousek, J., Gehrels, N., O'Brien, P., & Willingale, R. 2006, MNRAS, 369, 2059
 Panaiteescu, A., & Kumar, P. 2001, ApJ, 560, L49
 Panaiteescu, A., & Kumar, P. 2002, ApJ, 571, 779
 Panaiteescu, A., & Mészáros, P. 1999, ApJ, 526, 707
 Piran, T. 1999, Phys. Reports, 314, 575
 Piran, T. 2005, Reviews of Modern Physics, 76, 1143
 Piran, T., Shemi, A., & Narayan, R. 1993, MNRAS, 263, 861
 Piro, L., et al. 2005, ApJ, 623, 314
 Preece, R. D., Briggs, M. S., Mallozzi, R. S., Pendleton, G. N., Paciesas, W. S., & Band, D. L. 1998, ApJ, 506, L23
 Preece, R. D., Briggs, M. S., Mallozzi, R. S., Pendleton, G. N., Paciesas, W. S., & Band, D. L. 2000, ApJS, 126, 19
 Ramirez-Ruiz, E., & Fenimore, E. E. 2000, ApJ, 539, 712
 Razzaque, S., Mészáros, P., & Zhang, B. 2004, ApJ, 613, 1072
 Rees, M. J., & Mészáros, P. 1992, MNRAS, 258, 41P
 Romano, P., et al. 2006, A&A, 450, 59
 Sari, R., & Piran, T. 1997, ApJ, 485, 270
 Sari, R., & Piran, T. 1995, ApJ, 455, L143
 Sari, R., Piran, T., & Narayan, R. 1998, ApJ, 497, L17
 Sato, G., et al. 2007, ApJ, 657, 359
 Soderberg, A. M., et al. 2005, ApJ, 627, 877
 Tagliaferri, G., et al., 2005, Nature, 436, 985
 Usov, V. V. 1992, Nature, 357, 472
 Vietri, M., & Stella, L. 1998, ApJ, 507, L45
 Vietri, M., & Stella, L. 1999, ApJ, 527, L43
 Yamazaki, R., Toma, K., Ioka, K., & Nakamura, T. 2006, MNRAS, 369, 311
 Wang, X., & Loeb, A. 2000, ApJ, 535, 788
 Zeh, A., Klose, S., & Hartmann, D. H. 2004, ApJ, 609, 952
 Zhang, B., & Mészáros, P. 2002, ApJ, 581, 1236
 Zhang, B., & Mészáros, P. 2004, International Journal of Modern Physics A, 19, 2385
 Zhang, B., et al., 2006, ApJ, 642, 354
 Zhang, Z. B., Xie, G. Z., Deng, J. G., & Wei, B. T. 2007, Astronomische Nachrichten, 328, 99

TABLE 2
PARAMETERS FOR SIMULATED LIGHT CURVES^a

	A	B	C	D	E	F
E_0 (ergs)	10^{53}		10^{54}			
Redshift z	1					
k_θ	1		0.5			
Γ_0	300				100	
ϵ^b	0.2			0.002		
ϵ_{pk}^b	0.4					
R_1 (cm)	10^{16}				10^{17}	
R_2 (cm)	10^{17}				10^{18}	
r_1 (cm)	3×10^{12}	10^{13}	3×10^{12}	10^{13}		3×10^{13}
ξ	0.1					
ζ	0.1					

^aOnly the parameters changed from the previous column are listed.

^bReceived photon energy and ϵ_{pk} in units of $m_e c^2$.